THE ASTROPHYSICAL JOURNAL, 393:22–41, 1992 July 1

A HYDRODYNAMIC TREATMENT OF THE COLD DARK MATTER COSMOLOGICAL SCENARIO

RENYUE CEN AND JEREMIAH OSTRIKER
Princeton University Observatory, Princeton, NJ 08544
Received 1991 January 2; accepted 1992 January 7

ABSTRACT

The evolution of cold dark matter (CDM) models containing both baryonic matter and dark matter has been computed for a postrecombination Friedmann-Robertson-Walker universe utilizing a locally valid Newtonian approximation to model a representative piece of the universe whose size is much less than the horizon. Hydrodynamics is treated with a highly developed Eulerian hydrodynamic code. A standard Particle-Mesh (PM) code to calculate the motion of collisionless particles is coupled with this hydrodynamic code. We model the standard CDM scenario, adopting the parameters $h \equiv H_0/100$ km s^{-1} Mpc^{-1} = 0.5, $\Omega = 1.0$, $\Omega_b = 0.06$ with amplitude of the perturbation spectrum fixed by the requirement that $(\delta M/M)_{\rm rms} = 1/b = 1/1.5$ in a $8h^{-1}$ Mpc top hat sphere at $z = 0$. Four different boxes are simulated with box sizes of $L = (64, 16, 4, 1)h^{-1}$ Mpc, respectively, the smaller boxes providing good resolution but little valid information due to the absence of large scale power. We use $128^3 \sim 10^{6.3}$ baryonic cells and an equal number dark matter particles. In addition to the dark matter we follow separately six baryonic species (H, H$^+$, He, He$^+$, He^{++}, e^-) with allowance for both (nonequilibrium) collisional and radiative ionization in every cell. The background radiation field is also followed in detail with allowance made for bremsstrahlung and free-bound emission as well as ionization losses. However, in computing the thermal changes of the gas, we allow for both line and continuum processes as well as Compton interactions with the cosmic background radiation (CBR) and X-ray background radiation (XBR) fields. The mean final Zel'dovich-Sunyaev y parameter is estimated to be $\langle y \rangle = (1.3 \pm 0.6) \times 10^{-6}$, below currently attainable observations, with a rms fluctuation of approximately $\langle \delta y \rangle = (1.4 \pm 0.7) \times 10^{-6}$ on arcminute scales. Of greater interest, this model can make a nontrivial fraction of the soft X-ray background in the 0.1–1.0 KeV range. Comparing computations to observation we can set a limit for Ω_b of $\leq 0.037b^{2.2}$, which is consistent with the latest cosmic nucleosynthetic values. The model fails by a large factor to produce enough ionization either by shocks or radiation to satisfy the high-redshift Gunn-Peterson test. Addition of UV radiation from stars in forming galaxies may remedy this problem. We also examine the properties of X-ray emitting regions and the two-point correlation functions of the "galaxies"—the cooled, bound regions.

The rate of galaxy formation peaks at a relatively late epoch ($z < 1$). With regard to mass function, the smallest objects are stabilized against collapse by thermal energy: the mass-weighted mass spectrum peaks in the vicinity of $m_b = 10^{9.2}$ $M_\odot$ with a reasonable fit to the Schecter luminosity function if the baryon mass to blue light ratio is approximately 4.

Overall, the simulations provide strong support for the CDM scenario. Of particular interest is that, while the baryons are not biased on scales $\geq 1h^{-1}$ Mpc, the "galaxies" are, and that the "galaxies" have a correlation function of the required slope and the correct amplitude.

Subject headings: cosmology: theory — dark matter — hydrodynamics

1. INTRODUCTION

We have developed a three-dimensional computer code to model the evolution of structure in model universes containing both gaseous baryons and dark matter. In Cen (1992a) we described the method in detail. Here we turn to consideration of the popular CDM scenario addressed by us in preliminary fashion in Cen et al. (1990). With numerous improvements in the code, we are now able to calculate ionization state and radiative opacity in detail, thus computing far more accurately the background X-ray radiation field. Also, with a greatly improved treatment of gas heating and cooling, we can ask where galaxies are most likely to form, to identify such "galaxies" and to estimate galaxy correlation functions, multiplicity functions, etc. We can also ask, perhaps for the first time if there is a physical basis for "bias," the term used to describe an expectation that fluctuations in galaxy numbers are greater than fluctuations in total mass density.

This is not the place to provide a history of the CDM picture (cf. Peebles 1982; Blumenthal et al. 1988) or its present observational status. It appears that more large-scale power than is provided by the standard CDM picture is required to match observations of large-scale structure (cf. Vittorio, Juszkiewicz, & Davis 1986; Bond 1986; Peebles & Silk 1990; Maddox et al. 1990). But there are other important areas where models may be tested. Does the CDM spectrum have sufficient small-scale power to form high-redshift galaxies and to produce enough ionizing radiation at early enough times to be consistent with the observations of high-redshift quasars? The Gunn-Peterson (1965) test for high-redshift quasars, ($z = 4.897$, the observed highest redshift quasar to date; cf. Schneider, Schmidt, & Gunn 1991) provides an especially severe test. But we must also avoid producing so much hot gas as to violate the CBR isotropy measurements due to Zel'dovich-Sunyaev effect (Zel'dovich 1970, and references therein) and too much X-ray background radiation compared with the observations (Wu et al. 1990).

To date, tests of the popular CDM scenario on small scales appear to be quite successful. For example, the galaxy-galaxy two-point correlation function (cf. Park 1990) is in agreement with observations if dark matter density peaks are identified with galaxies after allowance for "bias." But we do not know if the assumption of bias is legitimate. Some internal structures of galaxies are also accounted for by CDM; for example, Frenk et al. (1998) reproduces both the form and the amplitude of the Tully-Fisher/Faber-Jackson relation if the galaxy luminosity is related to the rotational speed of the dark matter halo and the galaxy distribution is biased relative to the mass distribution in their N-body simulations. But the CDM model alone (i.e., without UV from star formation) may not be able to produce enough radiation to ionize the IGM (cf. Cen et al. 1990) if the galaxy distribution is biased over mass distribution with a bias factor bigger than unity. Our new results (not reported in this paper), utilizing a more advanced code including star formation indicate that with reasonable choices of efficiencies of UV and supernova processes from massive formed stars, the CDM model is able to ionize the IGM at an early enough time to satisfy the Gunn-Peterson test.

In this paper we will be able to address some of these questions on a physical basis. Our code does not have sufficient resolution to answer questions concerning details of galaxy formation. With $128^3 = 10^{6.3}$ cells and an equal number of dark matter particles, it permits a far more detailed analysis than was done in Cen et al. (1990) (primarily because we compute separately several atomic species in each cell) and provides far higher resolution than prior hydrodynamic analysis of CDM by Chiang, Ryu, & Vishniac (1989) and Ryu, Vishniac, & Chiang (1990). Despite the greater resolution of our code, compared to prior efforts, and the far more detailed treatment of the atomic physics given here, most of our conclusions must be offered tentatively with limits rather than values obtained for some important quantities.

The rest of the paper is organized in the following manner. Section 2 gives a brief description of the equations used (for a detailed description of equations and numerical techniques used, see Cen 1992a). Section 3 briefly describes the method to set up the initial conditions (see also Cen 1992a for a detailed description of the procedure to set up the initial conditions). Section 4 gives the results of the simulations. Section 5 concludes the paper.

2. EQUATIONS AND NUMERICAL TECHNIQUES

There are two sets of equations, one for the baryonic fluid and the other for collisionless dark matter particles. For the baryonic fluid we have eight time-dependent equations as follows: the mass conservation equation of total baryonic matter, the three ionization rate equations of H I, He I and He II, the three momentum equations in three directions, and the energy equation. Locally, we also satisfy charge conservation and the gas equation of state: $P = n_{\rm tot} kT$. The set of equations for the collisionless dark matter particles consists of three equations for change of momentum and three for change of position. In addition, we have the equation relating the density field to the gravitational forces, i.e., Poisson's equation for the perturbed density, and the two Einstein equations for the evolution of the cosmic comoving frame. Details of all the equations are presented in Cen (1992a).

The UV/X-ray radiation field (as a function of frequency and time) is calculated in a spatially averaged fashion. Changes in other quantities are computed each time step in each cell. Ionization, heating, and cooling are computed in a detailed non–LTE fashion.

In terms of numerical technique the dark matter evolution is computed with a standard PM code. The dark matter density and the gravitational forces exerted on dark matter particles are found using the cloud-in-cell ("CIC") algorithm (cf. Hockney & Eastwood 1981; Efstathiou et al. 1985; Cen 1992a). The gravitational potential, due to both baryons and dark matter, is calculated by solving Poisson's equation with periodic boundary conditions utilizing an efficient FFT algorithm.

Jameson's hydrodynamic code is described in greater detail in Jameson (1989) and references therein. We do not allow for energy input due to star formation in this simulation. As we have included such processes in subsequent work we can comment later on the effects of this omission. Simply put there is little effect on the large-scale velocity field and on high-temperature regions, but the omission of UV from stars does affect matter at smaller scales ($\Delta r < 5h^{-1}$ Mpc) and lower temperatures ($T < 10^5$ K).

It is important to recapitulate here what we have learned about the accuracy and spatial resolution of our hydrodynamical code. Detailed descriptions of a variety of tests are presented in Cen (1992a). Tests of known solutions for a shock tube indicate that pressure jumps are captured in three cells but density jumps are spread out over about four cells by our diffusive terms. Accurate computation of a one-dimensional caustic (Zel'dovich "pancake") as performed by Bond & Efstathiou (1984) and Shapiro & Struck-Marcell (1985) provides an especially severe test. We have reexamined the performance of the code subsequent to the publication of Cen (1992a) and made the following code revisions to accurately treat such very high Mach number shocks. Normally the code uses as a variable the total gas energy $E = U_{\rm th} + \frac{1}{2}\rho u^2$. Then changes in the thermal energy are calculated by subtracting from the change in E the change in $\frac{1}{2}\rho u^2$ as calculated from the momentum equation. This is inaccurate when $\frac{1}{2}\rho u^2/U_{\rm th} \gg 1$ as it is in much of the volume and especially in the region just outside of shocks in forming pancakes. We have altered the code to use the internal energy as variable away from shocks while maintaining the total energy within shocks. For a variety of technical reasons this reduces the diffusion in energy and increases overall accuracy. In a 128^3 adiabatic CDM run the total energy is conserved (utilizing the Layzer-Irvine check) to approximately 1%.

Of course as one imagines calculations made to higher and higher resolution, one would find higher and higher density fluctuations. But one can still ask, how would our calculation compare with a hypothetical perfect calculation which was rebinned to the level of our calculation? We tested this by running CDM runs of 128^3 cells, rebinning to 32^3 and comparing with the output of a 32^3 run. Such tests indicate that the average density fluctuation on the cell size is underestimated by about 30% for a 32^3 simulation declining to 15% at 128^3. In Cen (1992a) we attempt to determine the scaling with number of cells, of certain average quantities and find, for example, that for the average Zel'dovich-Sunyaev y parameter scaling to $N \rightarrow \infty$, *with fixed input spectrum* would increase $\langle y \rangle$ by approximately 40% with total bremsstrahlung emission increasing by about 60%. In the following sections we utilize such approximate extrapolation procedures, we hope cautiously, when they are appropriate, and in other cases we quote results as upper or lower limits.

We have underway, due to improvements in both software (shock capturing codes) and hardware, calculations which should increase our spatial resolution by approximately a factor of 2 over those results reported on here. There is one very important conclusion of this paper, with regard to the CDM model which we do not expect to be altered in the new work. One might naively expect that the smallest scales are the most unstable and that higher and higher resolution computation would show clumping on smaller and smaller scales. This, beyond a certain point, is not true. The CDM spectrum rises only quite slowly to small wavelengths and is easily stabilized by thermal motions since temperatures are easily maintained at $\sim 10^4$ K (the classic Jeans' Stability on small scales). This was shown analytically by Babul (1989) in linear theory. Our nonlinear computations confirm this. We see from our Table 5 that as the mass resolution scale is improved by a factor of 4096, the mass scale is only reduced by a factor of 12 and, at the resolution of our finest computation, the typical collapsing lump ($10^8\ M_\odot$) is well resolved. Preliminary work with higher resolution simulations confirms these results: the peak in the mass spectrum for CDM is approximately $10^{9.2}\ M_\odot$, and a Kolmogorov type divergence to smaller and smaller scales is not seen.

3. INITIAL CONDITIONS

The initial conditions adopted are those for Gaussian processes, i.e., the phases of the waves are random and uncorrelated. They are determined in the following manner: given the shape of the power spectrum $P(k)$ (see Fig. 1) for density fluctuations, the amplitude of the power spectrum is chosen to fit observations of galaxy clustering and of galaxy peculiar velocities. We adopt the method used by Weinberg & Gunn (1990), which is to normalize the power spectrum such that the mass fluctuations on a $8h^{-1}$ Mpc top-hat sphere is $1/b$ ($b = 1.5$ in the current simulation) at $z = 0$. The initial peculiar velocity field is then obtained by the Zeldovich approximation (cf. Zel'dovich 1970). For a detailed description of the method of setting up the initial conditions, see Cen (1992a). We adopt the transfer function for CDM given by Bardeen et al. (1986).

4. RESULTS

4.1. *Temperature and Density*

In the series of simulations described in this paper we computed the cosmic evolution of CDM models in a flat universe with the following set of parameters: $h = 0.5$, $\Omega = 1.0$, $\Omega_b = 0.06$, $b = 1.5$. The choice of $h = 0.5$ is conventional and gives a current age of about 14 billion yr. Using this and the light element nucleosynthesis determination of Walker et al. (1991) and Schramm (1991) $\Omega_b = 0.06h_{50}^{-2}$ we obtain our assumed value of Ω_b. Four different models are computed with box sizes of $L = (64, 16, 4, 1)h^{-1}$ Mpc, respectively. We use 128^3 cells with an equal number of dark matter particles in each of these simulations. Thus the nominal resolution in the four simulations ranges from $500h^{-1}$ Kpc in the largest box to $7.8h^{-1}$ Kpc in the smallest box with actual resolution in the hydro code perhaps a factor of 3 worse than this.

The larger scale simulations suffer most from the defects of insufficient resolution, the smaller scale simulations suffer from the lack of nonlinear long waves which would be truly present in the CDM model. Thus in the largest box we know that we are underestimating cooling and condensation of self-gravitating small-scale objects, whereas in the smallest box the omission of long waves makes the simulation not correct on average in that the gas will be less violently shaken and thus cooler than the average piece of the universe at that scale. Since temperatures are underestimated, the rate of condensation of self-gravitating objects is overestimated in this small box (as compared to the average). The reason for this is that the Jeans' mass at 10^4 K, where cooling decreases rapidly, is typically larger than the cell mass. We do not attempt to model specially those overdense regions where galaxies preferentially form. Thus, it is likely that our small boxes (since they have a density equal to the cosmic mean) underestimate the rate of galaxy formation in regions of high density, but they *overestimate* galaxy formation as compared to the average cosmic volume of that size.

The four simulations were run in the following order. First, we ran the $L = 16h^{-1}$ Mpc box simulation, since most of the radiation which is important for ionizing hydrogen and helium comes from the scales contained in the box for the CDM model. Our previous tests verified this point. Second, we ran the $L = 64h^{-1}$ Mpc box simulation with input radiation emissivity obtained from the $L = 16h^{-1}$ Mpc run. This, we consider the simulation providing the most useful results. Third, we ran the $L = 4h^{-1}$ Mpc box simulation with input radiation emissivities obtained from both the $L = 16h^{-1}$ Mpc and $L = 64h^{-1}$ Mpc runs. Last, we ran the $L = 1h^{-1}$ Mpc box simulation with input radiation emissivities obtained in all the previous three runs.

The reason we ran our models in the given order is as follows. The available computer power does not allow us to span the whole dynamical range needed to calculate all the quantities, but some additional information is obtained if we break the full range into several overlapping subranges. As we know, most of the ionizing radiation (UV and soft X-ray radiation) comes from the $(16\text{–}0.125)h^{-1}$ Mpc range, and photoionization is more effective than collisional-ionization under most conditions at the relevant densities. It is very important to include the correct amount of ionizing radiation, since all the cooling and heating processes depend sensitively on the ionization history of all species of the baryonic matter. Besides, the Gunn-Peterson test sets a limit as to when and how much hydrogen and helium of the IGM were ionized. Hence, in the $64h^{-1}$ Mpc simulation box, the ionizing radiation from the $16h^{-1}$ Mpc model must be added as an input emissivity to obtained the correct thermodynamic state of the gas. For the same reason we should include radiation from the two bigger boxes for smaller boxes runs, i.e., the $4h^{-1}$ Mpc and $1h^{-1}$ Mpc runs. Physically, this may be understood as follows. In a study of a small region there will be no massive X-ray emitting objects like the Coma clusters of galaxies, but gas in the small box is exposed to X-rays originating in a cluster outside the box. Our method allows us to include this in a spatially averaged fashion.

All the runs started at $z = 20$. As noted, the two small boxes $L = (4, 1)h^{-1}$ Mpc are useful only in a limited sense. After waves longer than the box size become nonlinear, calculations on these small scales have little validity. But they provide useful information nonetheless. The large scale (missing waves) would have heated the gas on smaller scales to higher temperatures than obtained when this long-wavelength power is missing (see Figs. 2*c* and 2*d* compared to Figs. 2*a* and 2*b*). Thus, formation of cooled bound objects on these small scales would have been *less* in a computation with still larger dynamic range than we have calculated in this paper. Since one

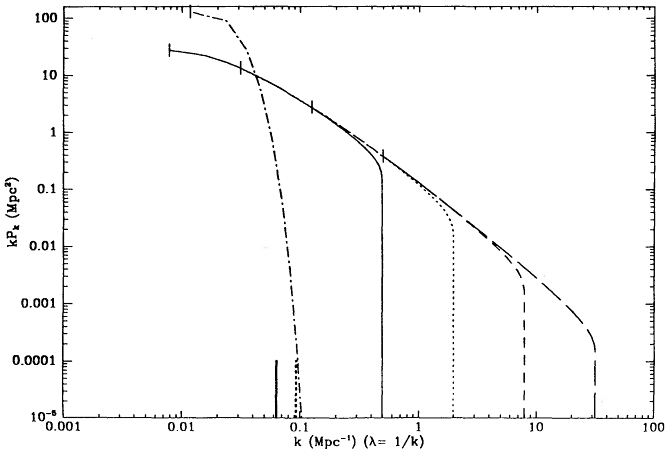

FIG. 1.—Actual initial power spectra in the simulations for the four CDM ($h = 0.5$, $b = 1.5$) models, $L = 64h^{-1}$ Mpc (*solid line*), $L = 16h^{-1}$ Mpc (*dotted line*), $L = 4h^{-1}$ Mpc (*short-dashed line*), $L = 1h^{-1}$ Mpc (*long-dashed line*). The dotted-dashed line (HDM spectrum, $h = 0.75$ and $b = 1$) is included for reference purposes. The thick solid label shows the place in the spectrum at $8h^{-1}$ Mpc, which we use to normalize the amplitude of the CDM spectrum, while the thick dotted label indicates that for the HDM spectrum.

of our main points is that most of the mass does not fragment into tiny lumps in the CDM picture, this point is strengthened by our inclusion of the small-scale boxes even if they only allow an upper bound to be put on the amount of mass of isolated small-scale structure. The countervailing tendency is to allow small-scale structure sitting on the peaks of larger wavelength perturbations to collapse more easily were larger scale power included. This is likely to be less important than the heating effect noted above, because the effects of long-wavelength power on temperature are likely to dominate over the density changes, leaving unaltered our original point that the calculations presented provide an upper bound on the formation of small, cooled objects. Higher resolution work, now in progress, should provide a more definitive answer.

Figure 1 shows the actual initial power spectra of the simulations for four CDM models linearly scaled to $z = 0$. The solid, dotted, short-dashed and long-dashed lines are the power spectra for theCDM models with box sizes $L = (64, 16, 4, 1)$, respectively. The HDM spectrum ($h = 0.75$, $b = 1.0$, *dot-dashed line*) is shown for reference purposes. The vertical thick solid label shows the place in the spectrum at $8h^{-1}$ Mpc which we use to normalize the amplitude of the CDM spectrum while the vertical thick dotted label indicates that for the HDM spectrum. We use an integral constraint on all waves longer than those at the marked label.

Now let us turn to the results obtained. The upper panels of Figures 2*a*–2*d* show the evolution of mean volume-weighted (*solid lines*), and mass-weighted (*dotted lines*) temperatures as a function of redshift. Also shown is the corresponding mean proper peculiar kinetic energy density (*dashed lines*) in units of Kelvin. The simulations are displayed in the following order: (*a*) $L = 64h^{-1}$ Mpc, (*b*) $L = 16h^{-1}$ Mpc, (*c*) $L = 4h^{-1}$ Mpc, (*d*) $L = 1h^{-1}$ Mpc (this order is maintained in subsequent figures). We see that, in the simulation with box size $L = 64h^{-1}$ Mpc, the final mean mass-weighted temperature exceeds 10^6 K representing the small fraction of strongly shock-heated gas in regions like the Coma cluster of galaxies. In the smaller boxes, $L = 4$, and $1h^{-1}$ Mpc, the mean temperatures stay at about 10^4 K because cooling processes (mainly the hydrogen and helium collisional excitation cooling processes) are important and the cooling time is short compared with the Hubble time, so baryonic matter can be shocked and then cooled to remain at these temperatures. Besides, the shocks on these smaller scales are less strong (due to omission of waves larger than its box size, some of which would have entered the nonlinear regime at $z = 0$ if they were present) compared with those in the bigger boxes, where shock heating heats baryonic matter to temperatures $\geq 10^6$ K.

This result can be understood easily, since the final shock-heated temperatures are about $v^2 m_H/k$, where v is the shock incident velocity, $v \propto Hr$, and r is the relevant scale ($\sim \lambda$). Thus $T \sim v^2 m_H/k \sim 10^6$ K for scale $1h^{-1}$ Mpc and $T \sim v^2 m_H/k \sim 10^4$ K for scale $0.1h^{-1}$ Mpc. Consequently the reason that the mean temperatures gradually increase is that, as longer and longer wavelength scales become nonlinear with increasing time, $T(t \sim [\lambda_{\rm nonlinear}(t)H(t)]^2(m_H/k)$. Because $\lambda_{\rm nonlinear}(t) \propto t^\alpha$, and α is about 1.5 for CDM, given that $H(t) \propto t^{-1}$, one expects $T(t)$ to be an increasing function of time. For a limited piece of the universe of size R (i.e., fixed comoving box size), after a certain epoch all waves $\lambda < R$ have gone nonlinear and there exist no waves, of course, with $\lambda > R$, so adiabatic cooling takes over and the temperature will decline (in the absence of other processes). This artificial saturation is seen in the smallest box (see Fig. 2*d*).

The lower panels of Figures (2*a*–2*d*) show the evolution of the variances of the baryonic and dark matter density on the scale of the cell size of each simulation, which are defined as

$$\sigma_M^2 \equiv \langle \rho^2 \rangle / \langle \rho \rangle^2 - 1 . \quad (1)$$

Here $M = (d, b)$, σ_d is the dark matter density variance, and σ_b is the baryonic matter density variance. In the bigger boxes the dotted line (*dark matter*) shows higher fluctuations. In the smaller boxes the gas component (*solid line*) has higher fluctuations. We define a bias factor as follows:

$$b(\Delta l) \equiv \frac{\sigma_b(\Delta l)}{\sigma_d(\Delta l)} . \quad (2)$$

We find that on scales $\lesssim 0.125h^{-1}$ Mpc, cooling processes are important, which leads to the "biased" formation of overdense baryonic objects: baryonic matter is more clumpy than dark matter on these scales. But for larger scales, cooling processes are not significant enough at later times to play an important role. Therefore, we find that on scales larger than $0.125h^{-1}$ Mpc, the situation is just the opposite, i.e., dark matter is more clumpy than baryonic matter. Finally, we expect that on very large scales these two different kinds of matter should not be biased with respect to each other. The reason is that pressure is insignificant on these scales, therefore baryonic matter should act just like dark matter particles, i.e., gravitational forces are all that is relevant for both components.

Hence, we conclude that around $0.125h^{-1}$ Mpc dark matter and baryonic matter should have about the same clumpiness, i.e., baryonic matter will follow the dark matter distribution. These results are consistent with those of Yuan, Centrella, & Norman (1991, their Fig. 2*a*). Note that this is different from saying that the galaxy distribution follows (or does not follow) the mass distribution, since the baryonic mass distribution is significantly different from the galaxy distribution.

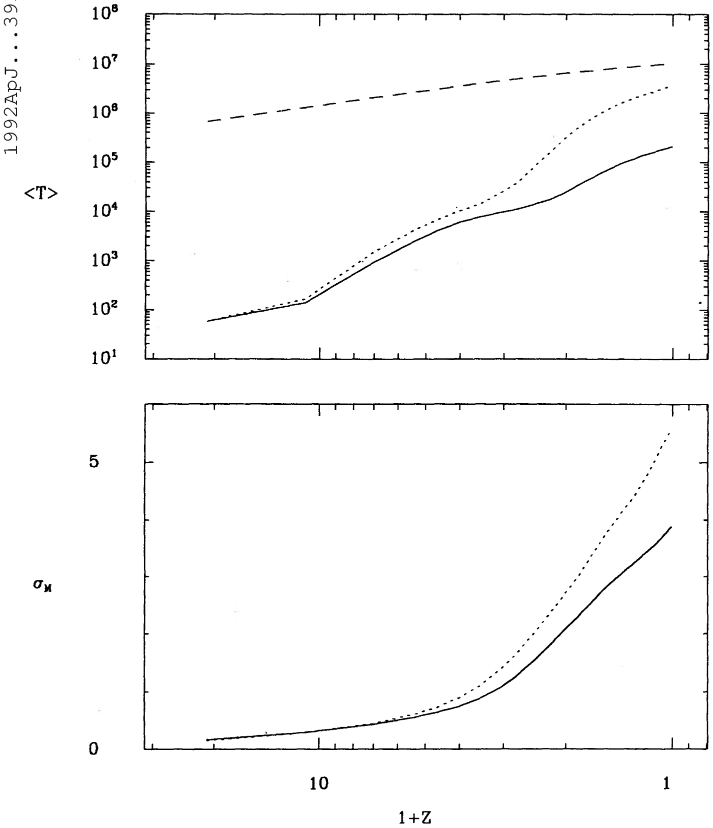

FIG. 2a

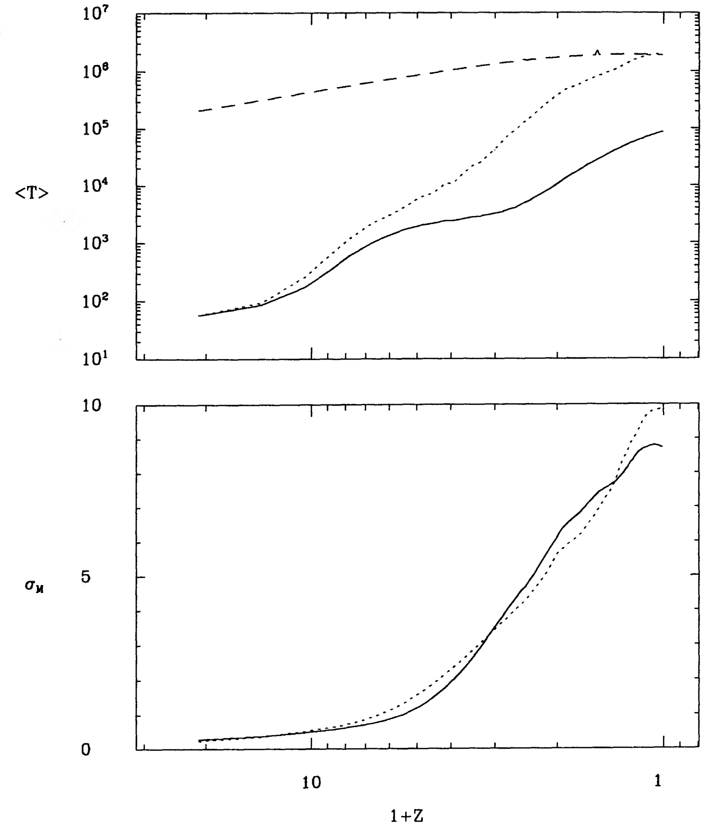

FIG. 2b

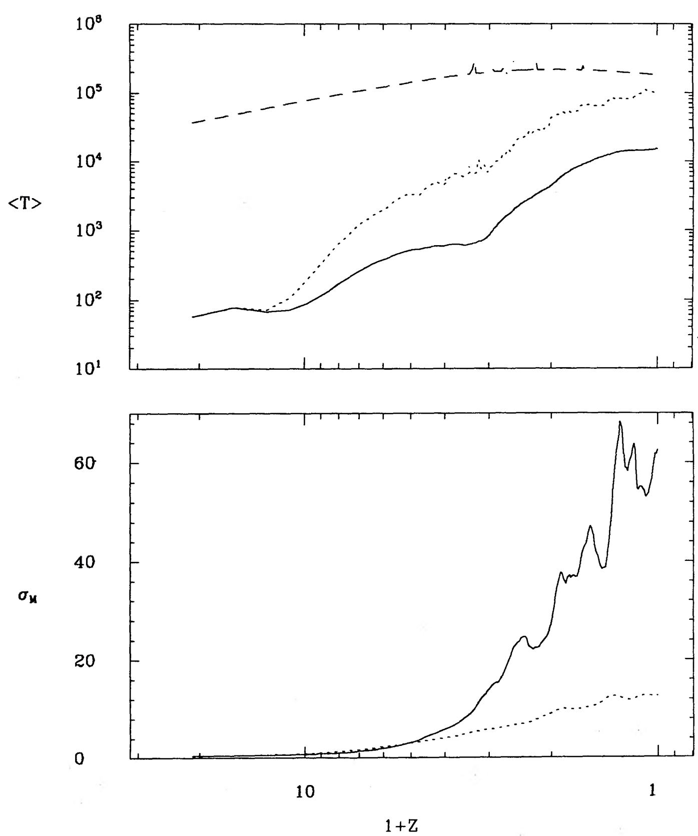

FIG. 2c

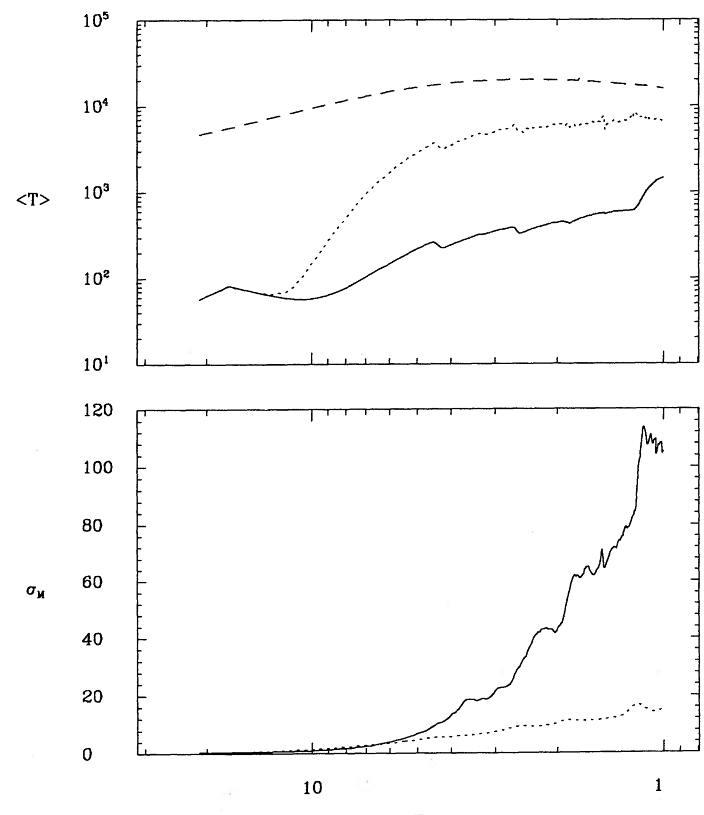

FIG. 2d

FIG. 2.—Upper panels of Fig. 2*a*–2*d* show the evolution of mean volume-weighted (*solid lines*), and mass-weighted (*dotted lines*) temperatures as a function of redshift. Also shown is the corresponding mean proper peculiar kinetic energy density (*dashed lines*) in units of Kelvin. The lower panels show the density variances of baryonic matter (*solid line*) and dark matter (*dotted line*) (see eq. [1] for definitions).

Contrary to naive expectations, there is not continually more and more clumping on smaller and smaller scales, even in our simulations in which the temperature in the smallest boxes is known to be too small because larger waves should have been included. The two smallest boxes show comparable growth in σ, and we estimate that the maximum clumping occurs on scales intermediate of perhaps 20 kpc which corresponds to a mass scale of $10^{8.5}$ $M_\odot$. The reason that still smaller scales are not more unstable is the usual one. Since gravity is a long-range force, small mass scales are stabilized relatively easily by thermal motions. A 10 kpc wave becomes nonlinear at a redshift of $z = 8$ with our normalization. The corresponding potential fluctuation is $\delta\phi_{\rm rms} = 3.0^2(\mathrm{km\ s^{-1}})^2$, which corresponds to a temperature of only 363 K. For the relatively flat CDM spectrum a small number of nonlinear waves at the 20–30 kpc wavelength thus heats up the material to the point where the 10 kpc waves are stable (cf. Babul 1989). This fact, the relative stability of small scales, is the primary new result learned from the small box simulations.

Figures 3*a*–3*d* show the volume-weighted histograms of temperatures of cells at four epochs. Figures 4*a*–4*d* show the mass-weighted histograms of temperatures of cells at the same epochs. One may note that for the model with box size $L = 64h^{-1}$ Mpc, at early epochs ($z > 2$), most of the cells as well as most of the volume stay at low temperatures, $T \leq 10^4$ K. At epochs between $z = 2$ to $z = 1$, a large fraction of the volume and even larger fraction of the mass has temperatures about about 2×10^4 K due to the hydrogen collisional excitation cooling. After $z = 1$, cooling becomes less important on this scale, and baryonic matter is gradually heated up by shocks as well as the ionizing radiation field. This leaves most of the mass at high temperatures $T \geq 10^5$ K, with 10% of mass reaching temperatures above 10^7 K, although these regions contain only a very small fraction of total volume.
For the model with box size of $L = 1h^{-1}$ Mpc, at $z \geq 5$, only a very small fraction of mass is hotter than 10^4 K. At $z = 2$ most of the mass has been heated up to 10^4 K although it only occupies a small fraction of the volume. As evolution continues, cells heated to this equilibrium temperature remain there, and more and more cells are heated and join this fraction. But by $z = 0$, there is still no region hotter than 10^5 K. This is due to the fact that hydrogen and helium collisional excitation cooling processes are always important on these small scales; baryonic matter on these scales is relatively weakly shocked (never being shock-heated to above 10^6 K), and the long-wavelength waves that would heat the gas to high temperatures are artificially absent from the small boxes. For the models with intermediate box sizes, $L = 16, 4h^{-1}$ Mpc, the situation lies between these two extreme cases.

Figures 5*a*–5*d* show some typical slices with contours of baryonic matter density, dark matter density and baryonic matter temperature at $z = 2$, 0. Notice that linear structures are more visible in the gas than in the dark matter. These structures arise from the intersection of sheets ("pancakes") with our displayed slices. In the dark matter we expect that perturbations with $\boldsymbol{k}$ vectors within the pancakes will be relatively unstable. Note also that in Figure 5*a*, which shows matter on a large scale, the dark matter is more concentrated than the baryons, whereas in Figure 5*d*, on small scales, the baryons are more clumped.

Figures 6*a*–6*d* show the (ρ, T) contour plots. The innermost contours represent conditions of density and temperature in the most common cells at $z = 0$. Note that the smaller boxes have certain regions with very high densities ($\rho/\langle\rho\rangle > 10^3$) but relatively low temperatures (10^4–10^5 K) while for bigger boxes this feature disappears. The four dotted lines in Figure 6*d* from left to right show the fraction of neutral hydrogen at 10^{-4}, 10^{-3}, 10^{-2} and 10^{-1}. Low-density gas is ionized relatively early and remains ionized due to the long recombination time at late epochs. Notice that in the largest ($64h^{-1}$ Mpc) box the most dense gas is also the hottest and has roughly the characteristics of the gas in the center of the Coma cluster. On all scales the most common cells have a density $\rho/\bar{\rho} \simeq 0.1$ and are in "voids."

4.2. *Volume and Mass Distributions*

To be able to see the situation more clearly, we analyze the results in another useful way. We arbitrarily divide the baryonic matter into four components: (1) virialized, bound, hot objects, which on the large scales represent the gas in clusters of galaxies and on the small scales represent the L_α clouds—"Virialized Gas"; (2) bound, cooled objects, i.e., collapsed compact objects—"Galaxies;" (3) unbound, hot regions with temperature $\geq 10^5$ K—"Hot IGM;" (4) other regions, primarily—"Voids." The break point at 10^5 K is adopted because it is past the peak of the "cooling curve."

A virialized object (1) satisfies the following conditions: $M_B > M_J$, $M_{\rm tot} > q\langle M_{\rm tot}\rangle$, $\nabla \cdot \boldsymbol{u} < 0$ and $t_{\rm cool} > t_{\rm dyn}$; where M_B is the baryonic mass in the cell, $\langle M_{\rm tot}\rangle$ is the average total mass in a cell, $M_{\rm tot}$ is the total mass in the cell, $\boldsymbol{v}$ is the proper peculiar velocity, and q is an overdensity factor, which we take to be 10 (this is quite arbitrary and is used as a computational convenience, so that the more detailed criteria need only be calculated for a small number of cells). The Jeans' mass M_J for a cell is defined as follows:

$$M_J \equiv G^{-3/2}\rho_b^{-1/2}C^3\left[1 + \left(\frac{\delta\rho_d/\langle\rho_d\rangle}{\delta\rho_b/\langle\rho_b\rangle}\right)\left(\frac{\langle\rho_d\rangle}{\langle\rho_b\rangle}\right)\right]^{-3/2}, \quad (3)$$

where ρ_b and ρ_d are the proper baryonic and dark matter densities in the cell, respectively; $\langle\rho_b\rangle$ and $\langle\rho_d\rangle$ are the mean proper baryonic and dark matter densities, respectively; G is the gravitational constant; and C is the local adiabatic speed of sound. The dynamical time of the cell is defined as

$$t_{\rm dyn} \equiv \sqrt{\frac{3\pi}{32G\rho_{\rm tot}}}, \quad (4)$$

where $\rho_{\rm tot} \equiv \rho_b + \rho_d$ and the cooling time of the cell $t_{\rm cool}$ is defined as

$$t_{\rm cool} \equiv \left(\frac{P}{\gamma - 1}\right)\left(\frac{1}{\Lambda}\right), \quad (5)$$

where Λ is the net integrated cooling rate due to all the relevant cooling and heating processes in the cell (cf. Cen 1992a for details) and γ is the ratio of specific heats. Thus our definition of "virialized gas" (1) is appropriate for regions like the great clusters where there exists a gravitationally bound volume of gas which is too hot to cool on the relevant time scale.

Next, we can use our criteria to pick out overdensity contracting regions which are cooling rapidly, and are unstable to collapse and form bound objects. Thus objects (2) are defined as follows: $M_B > M_J$, $M_{\rm tot} > q\langle M_{\rm tot}\rangle$, $\nabla \cdot \boldsymbol{u} < 0$, and $t_{\rm cool} < t_{\rm dyn}$ (or $T \leq 10^4$ K). The last inequality implies that we consider the regions having temperatures less than 10^4 K to be able to cool by other processes such as molecular cooling (not included in our calculations).

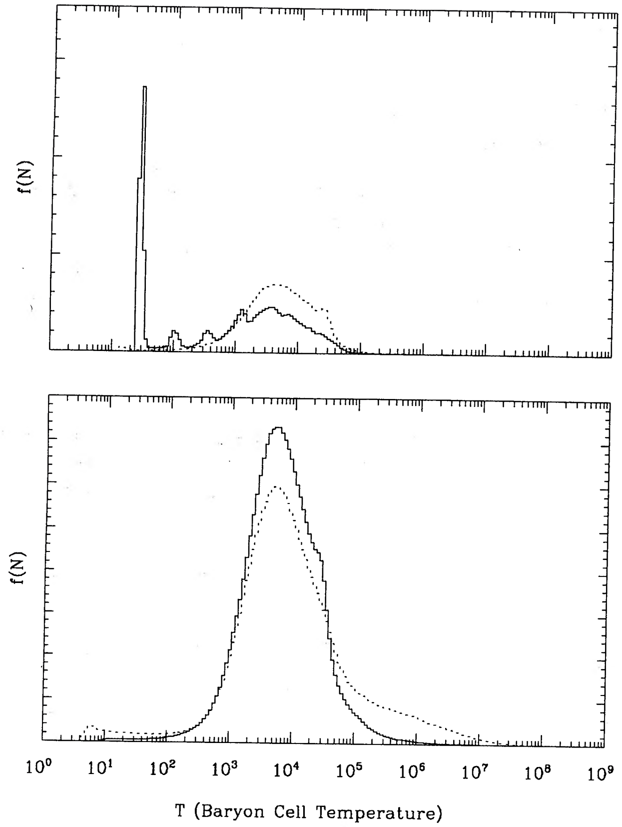

FIG. 3*a*

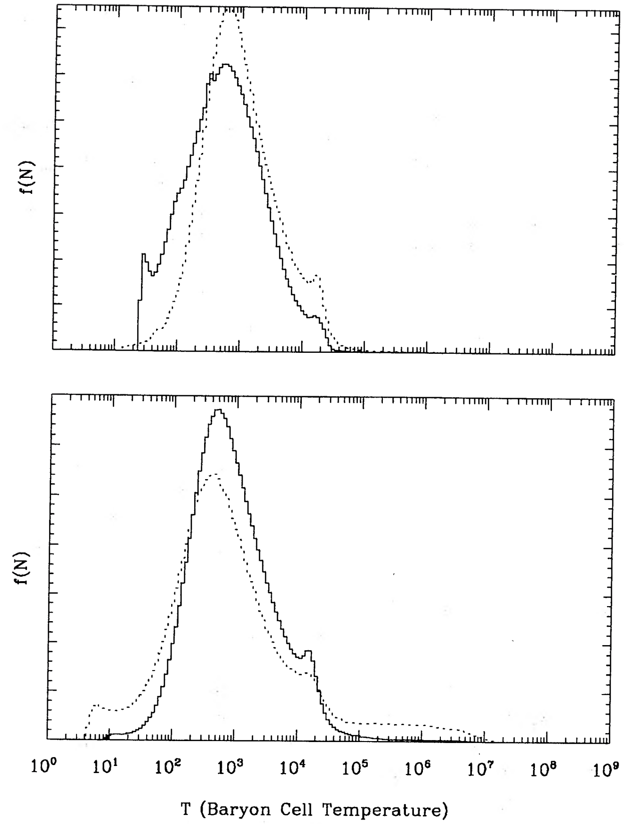

FIG. 3*b*

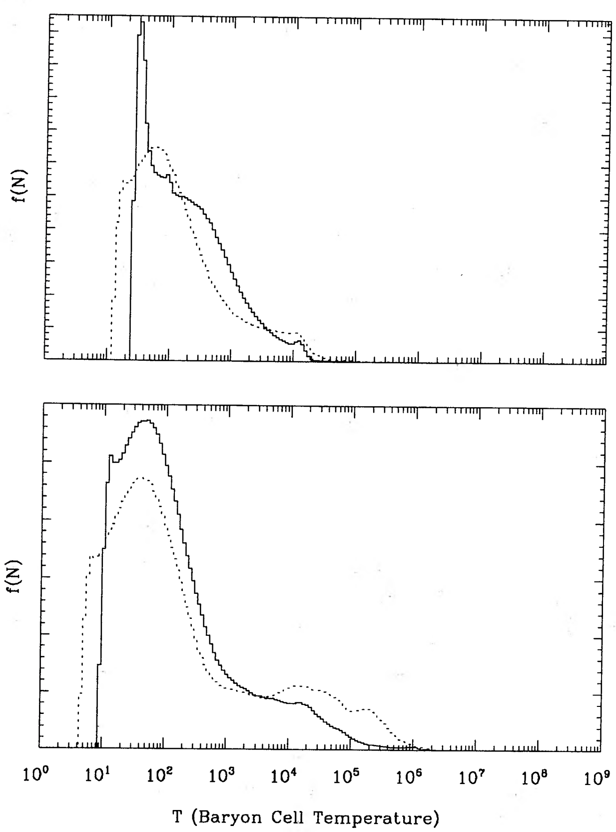

FIG. 3*c*

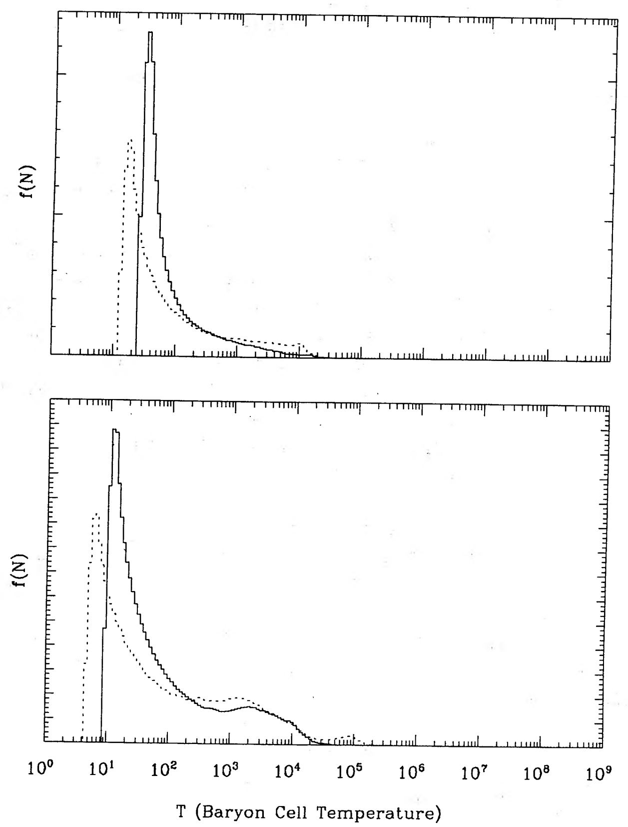

FIG. 3*d*

FIG. 3.—Volume-weighted histograms of temperatures of cells at several epochs, at $z = 5$ (*solid line, upper panel*), $z = 2$ (*dotted line, upper panel*), $z = 1$ (*solid line, lower panel*) and $z = 0$ (*dotted line, upper panel*). The peaks at $T \sim 10^{4.5}$ K are mainly due to cooling by hydrogen L_α lines. The temperature rises in the bigger boxes at late times are due to the ultimate breaking of long waves.

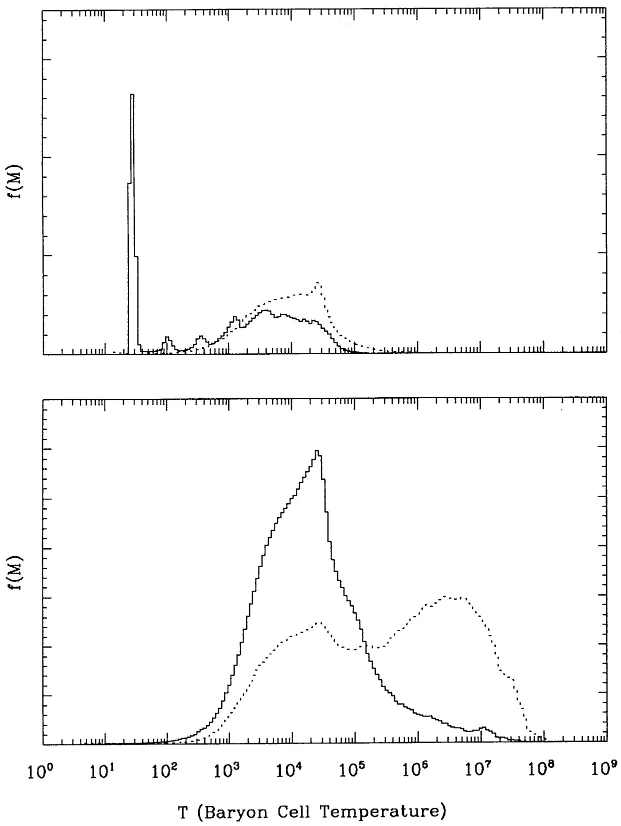

FIG. 4*a*

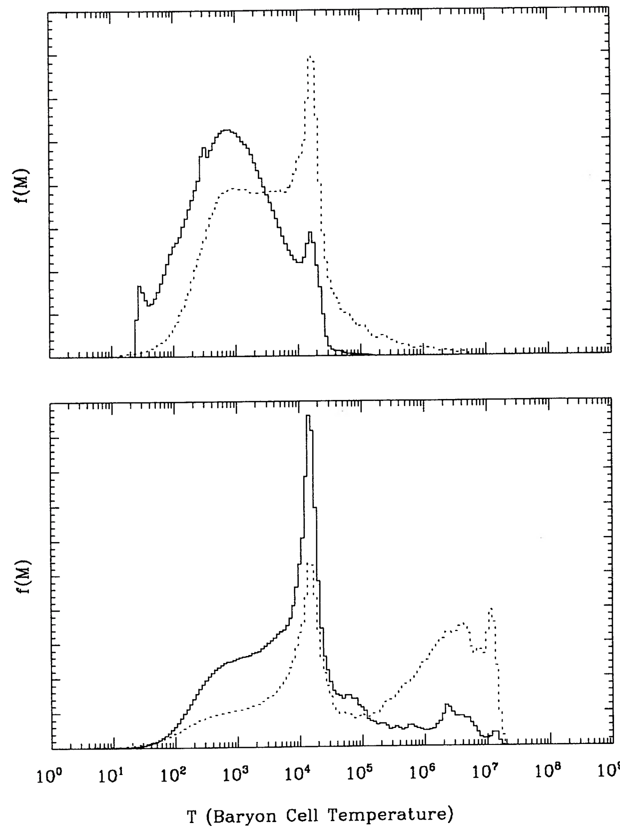

FIG. 4*b*

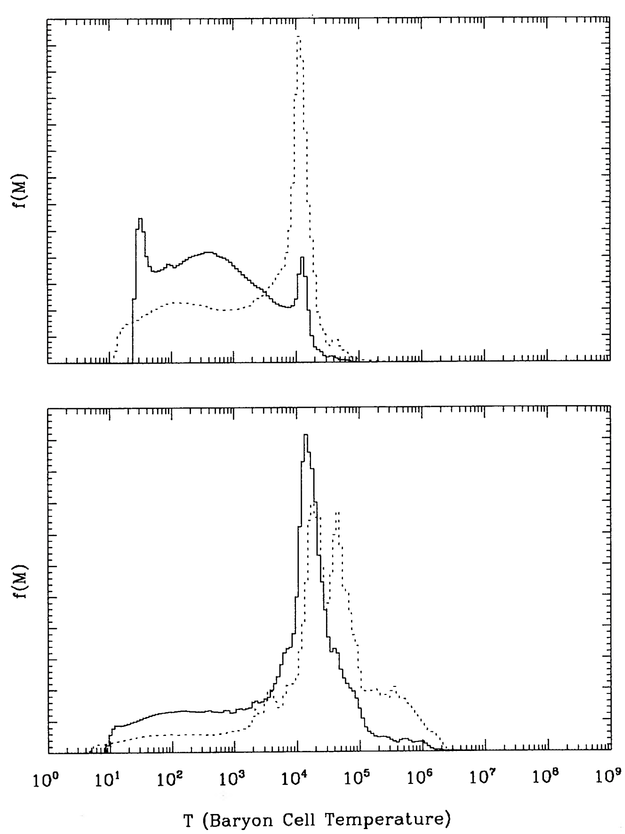

FIG. 4*c*

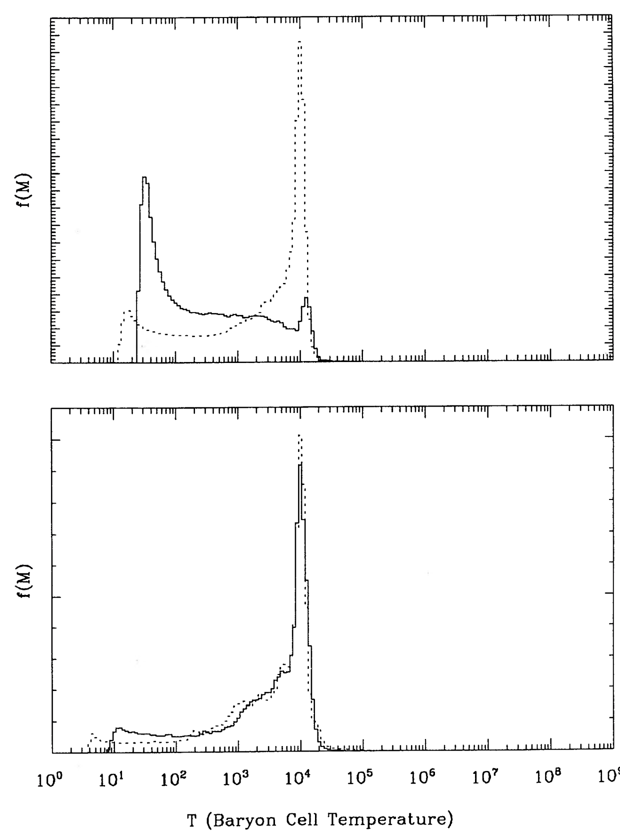

FIG. 4*d*

FIG. 4.—Mass-weighted histograms of temperatures of cells at several epochs, at $z = 5$ (*solid line, upper panel*), $z = 2$ (*dotted line, upper panel*), $z = 1$ (*solid line, lower panel*) and $z = 0$ (*dotted line, lower panel*). In the big box shock-heating brings 10% of gas to temperatures exceeding 10^7 K.

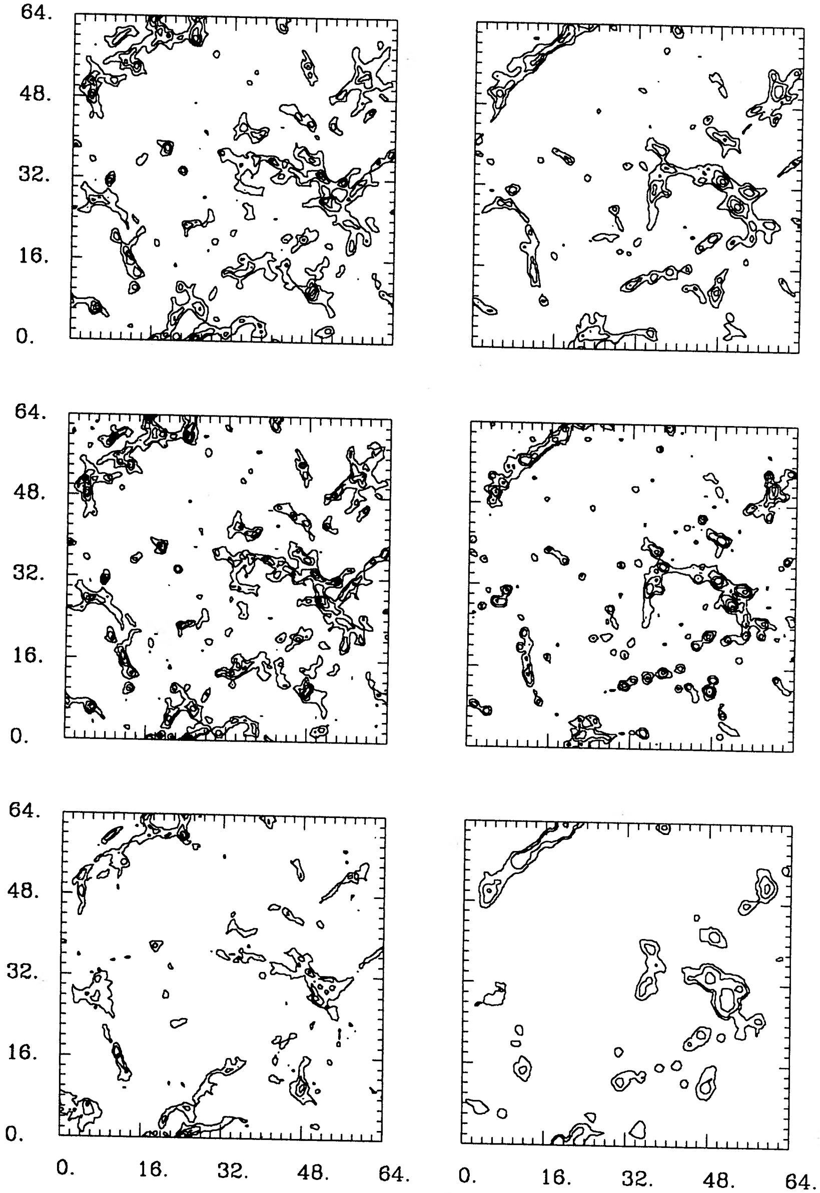

FIG. 5a

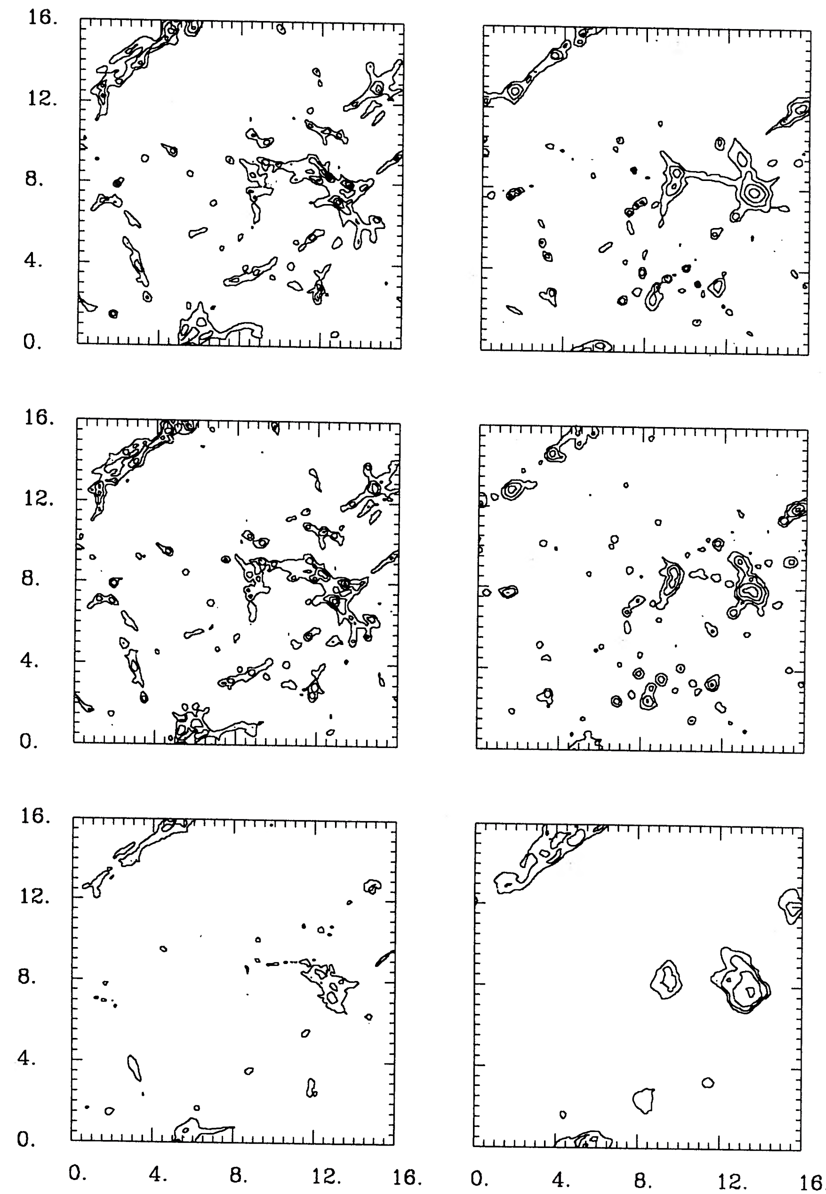

FIG. 5b

FIG. 5.—Some typical slices of baryonic matter density (*upper panels*), dark matter density (*middle panels*) and baryonic matter temperature (*lower panels*) contour plots at $z = 2$ (*left*) and $z = 0$ (*right*) for simulations with $L = 64, 16, 4, 1h^{-1}$ Mpc, respectively. All slices are 21 cells thick. The contour levels for densities are as follows: $[1 + \sigma(\rho_b)]^{I/2}$ for $L = 64h^{-1}$ Mpc and $L = 16h^{-1}$ Mpc boxes, $[1 + \sigma(\rho_b)]^{I/4}$ for $L = 4h^{-1}$ Mpc and $L = 1h^{-1}$ Mpc boxes, with $\sigma(\rho_b)$ the density rms fluctuation in the baryonic matter. The contour levels for temperature are as follows: $[1 + \sigma(T)^{I/2}$ for $L = 64h^{-1}$ Mpc and $L = 16h^{-1}$ Mpc boxes, $[1 + \sigma(T)]^{I/4}$ for $L = 4h^{-1}$ Mpc and $L = 1h^{-1}$ Mpc boxes, with $\sigma(T)$ the temperature rms fluctuation in the baryonic matter; where I is positive integer, $\sigma(\rho_b)(z = 2) = 1.1, 3.5, 14., 21.$, $\sigma(\rho_b)(z = 0) = 3.9, 8.7, 62., 105.$, $\sigma(T)(z = 2) = 2.5, 7.8, 8.8, 4.4$, $\sigma(T)(z = 0) = 6.9, 6.9, 5.4, 6.1$, respectively, for $L = 64, 16, 4, h^{-1}$ Mpc boxes.

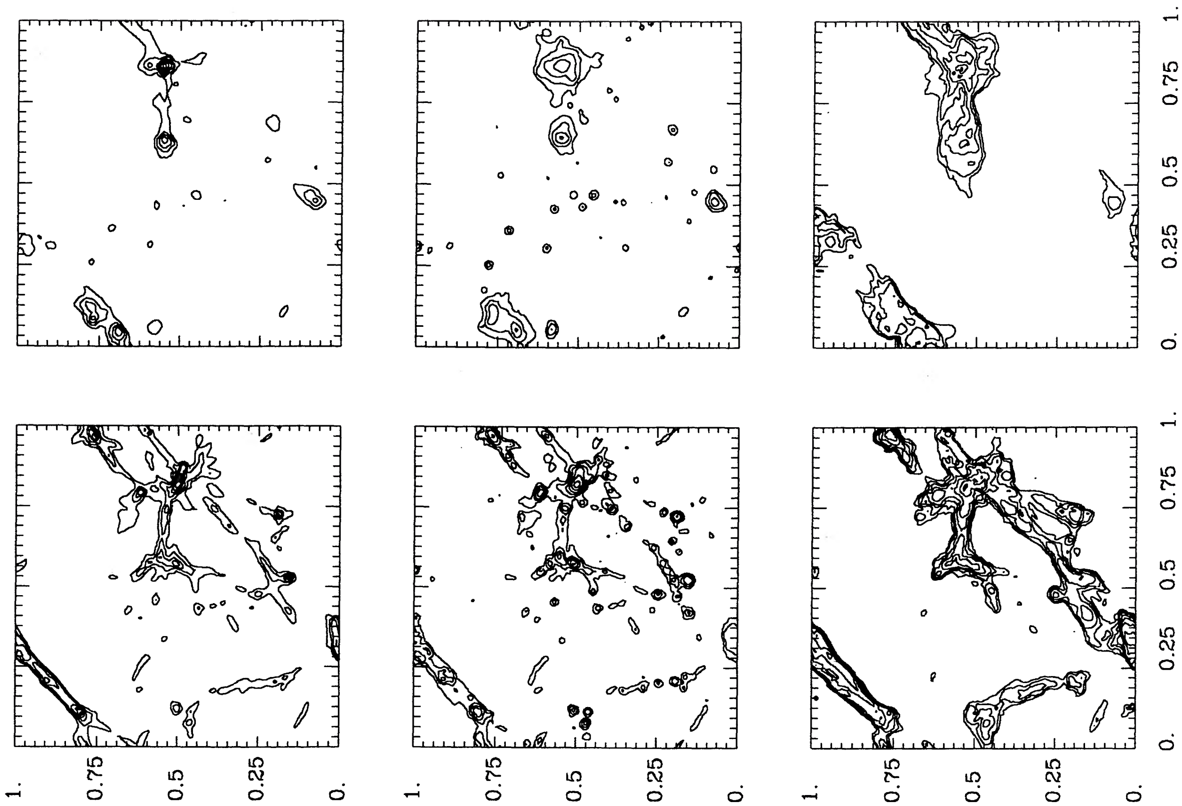

FIG. 5d

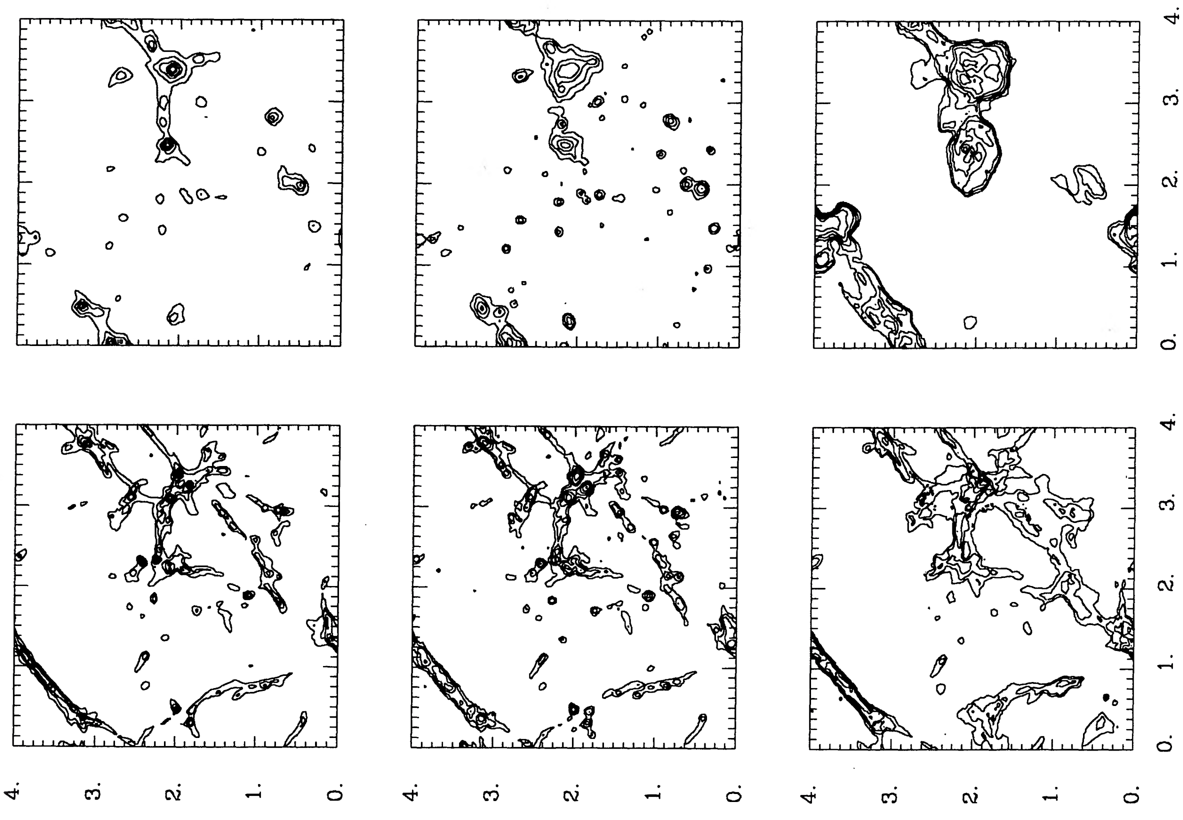

FIG. 5c

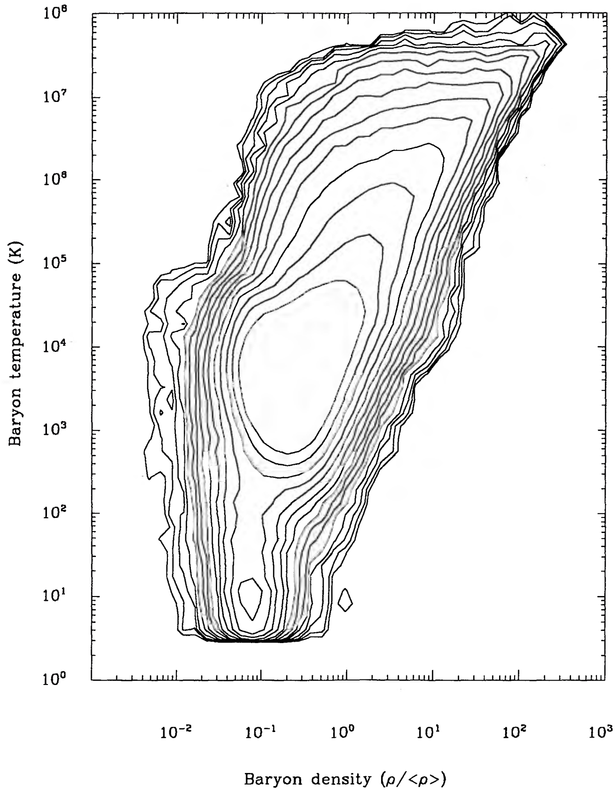

FIG. 6*a*

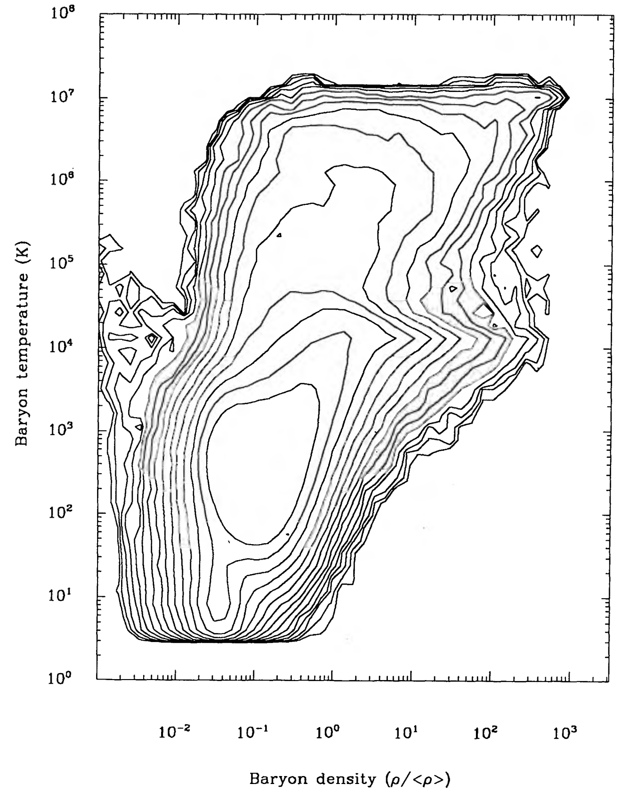

FIG. 6*b*

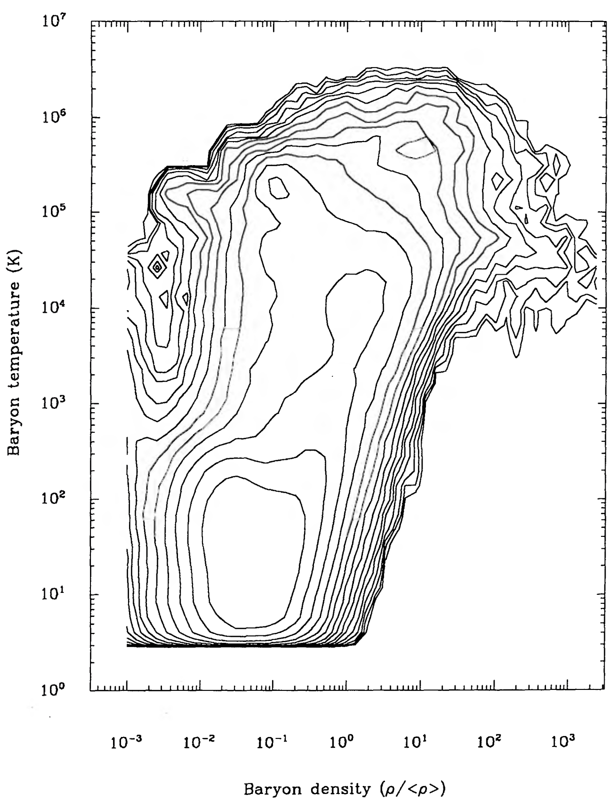

FIG. 6*c*

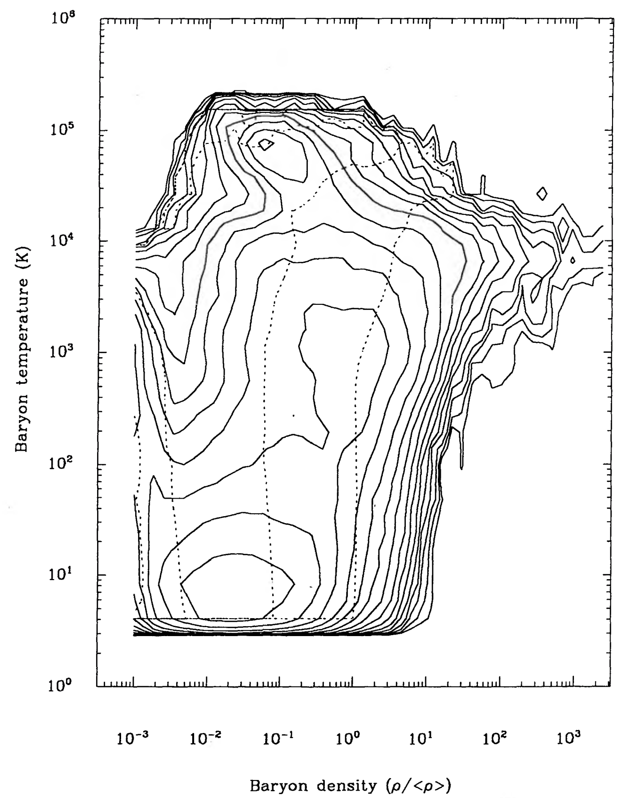

FIG. 6*d*

FIG. 6.—(ρ, T) contour plots. The innermost contours represent the highest fraction of cells in terms of volume with these densities and temperatures at $z = 0$. Note that the smaller boxes have certain regions with high densities but relatively low temperatures while for bigger boxes this feature disappears. The contour levels are defined as follows: $10(I/4)$, where I is positive integer, $I = 0$ corresponds to the outermost contour, and contours inside it have gradually increasing I. The four dotted lines in Fig. 6*d* from left to right show the fraction of neutral hydrogen at 10^{-4}, 10^{-3}, 10^{-2} and 10^{-1}.

TABLE 1

SUMMARY OF FRACTIONS IN THE $L = 64h^{-1}$ Mpc BOX MODEL

Redshift	Z 10	5	3	2	1	0
A. Volume-Weighted Fractions						
(1) "Virialized Gas"	0.	0.000000	0.000000	0.000000	0.000005	0.000005
(2) "Galaxies"	0.	0.000002	0.000249	0.001048	0.002096	0.000314
(3) "Hot IGM"	0.	0.000095	0.000676	0.004104	0.025887	0.120036
(4) "Voids"	1.	0.999903	0.999075	0.994848	0.972912	0.879638
B. Mass-Weighted Fractions						
(1) "Virialized Gas"	0.	0.000000	0.000000	0.000000	0.000040	0.000039
(2) "Galaxies"	0.	0.000014	0.002515	0.012394	0.026839	0.002168
(3) "Hot IGM"	0.	0.000359	0.003567	0.024287	0.152565	0.606379
(4) "Voids"	1.	0.999627	0.993917	0.963318	0.820564	0.391315

Objects of the third and fourth types consist of the remaining regions, with temperature $\geq 10^5$ K being classified as the third component and with temperature $< 10^5$ K as the fourth component. These four components make a complete set of possible objects and each cell is classified accordingly. In Tables 1–4 we list the volume and mass-weighted fraction of these four components at five epochs, $z = 10, 5, 2, 1, 0$, for the four different runs with box sizes, $L = (64, 16, 4, 1)h^{-1}$ Mpc. In these tables we do not treat "galaxy formation" as irreversible, which it would be were a true stellar component to be formed. Thus, fewer cells satisfy our criterion to be "galaxies" after $z = 1$ than at that epoch (except for Tables 3B and 4B).

Now let us look at the properties of the typical collapsed objects of the four boxes at redshift $z = 1$. The somewhat suprising results are shown in Table 5. We note that the mass fraction of collapsed objects has peaked at somewhere between the $L = 16h^{-1}$ Mpc and $L = 4h^{-1}$ Mpc boxes. This corresponds to average baryonic mass of collapsed objects lying between $\langle m \rangle = 1.1 \times 10^9\ M_\odot$ per cell to $\langle m \rangle = 1.8 \times 10^9\ M_\odot$ per cell in the range appropriate for normal dwarf galaxies. This shows that the collapsed fraction saturates on this scale; as noted earlier, the very small mass scales covered by the $1h^{-1}$ Mpc box are not more unstable than those in the $4h^{-1}$ Mpc box. In a better calculation, with all the longer waves included, the collapsed fraction would clearly peak at a still larger scale since the temperature and hence Jeans' mass would be higher. In addition, extra energy input from star formation, were it included, would also increase the temperature and further stabilize small scale perturbations. Notice also that at $z = 0$ the ratio of the mass in "Galaxies" to "Virialized Gas," is smallest in the smallest box, not the largest, as might initially have been expected. On all scales the largest fraction of the mass is in the IGM with comparable fraction in the warm ("Voids") and hot ("Hot IGM") components.

Ryu et al. (1990) performed a CDM simulation with 32^3 cells and an equal number of dark matter particles. They chose a box size of $9h^{-1}$ Mpc, with $\Omega_b = 0.1$, so the cell size of their simulation is somewhere between our $L = 64h^{-1}$ Mpc and $L = 16h^{-1}$ Mpc boxes. They included energy feedback into IGM from forming galaxies. Under these conditions they found that galaxies started to form when $z \sim 20$, and reached a maximum formation rate at $z \sim 9$. After that, the rate decreased until $z \sim 2$ and then increased again up to the present. In our simulations we found that the galaxy size systems were formed mostly during the period of $z = 2$ to $z = 1$. Two factors could contribute to the differences between our models and their model. The first is the energy feedback mechanism they used, which heated up the IGM after early galaxy formation and hence suppressed formation of galaxies during the subsequent period ($z = 9$ to $z = 2$). The second is the more easily satisfied galaxy-formation criteria they adopted, mainly the lower overdensity requirement (5.5 in their

TABLE 2

SUMMARY OF FRACTIONS IN THE $L = 16h^{-1}$ Mpc BOX MODEL

Redshift	Z 10	5	3	2	1	0
A. Volume-weighted Fractions						
(1) "Virialized Gas"	0.	0.000039	0.000238	0.000465	0.000715	0.000379
(2) "Galaxies"	0.	0.000495	0.001966	0.002865	0.002969	0.000678
(3) "Hot IGM"	0.	0.000012	0.000366	0.001484	0.006697	0.054848
(4) "Voids"	1.	0.999454	0.997428	0.995183	0.989619	0.944096
B. Mass-Weighted Fractions						
(1) "Virialized Gas"	0.000000	0.000319	0.002153	0.005224	0.010364	0.009062
(2) "Galaxies"	0.000002	0.005176	0.028089	0.050389	0.071574	0.028397
(3) "Hot IGM"	0.000000	0.000123	0.011525	0.042528	0.137770	0.511957
(4) "Voids"	0.999998	0.994383	0.958228	0.901858	0.780291	0.450584

TABLE 3

SUMMARY OF FRACTIONS IN THE $L = 4h^{-1}$ Mpc BOX MODEL

Redshift	Z 10	5	3	2	1	0
A. Volume-Weighted Fractions						
(1) "Virialized Gas"	0.000085	0.000519	0.000403	0.000175	0.000046	0.000007
(3) "Galaxies"	0.000000	0.000342	0.000432	0.000228	0.000075	0.000012
(3) "Hot IGM"	0.000000	0.000001	0.000054	0.000495	0.007158	0.034546
(4) "Voids"	0.999914	0.999138	0.999111	0.999101	0.992720	0.965423
B. Mass-Weighted Fractions						
(1) "Virialized Gas"	0.000556	0.004288	0.005614	0.001531	0.001570	0.001570
(2) "Galaxies"	0.000005	0.008885	0.031513	0.048792	0.080898	0.064696
(3) "Hot IGM"	0.000000	0.000125	0.000582	0.002762	0.052298	0.233360
(4) "Voids"	0.999439	0.986703	0.962291	0.946915	0.865235	0.699441

case compared to 10 in our case). Finally the net cooling in their code was considerably larger than in ours, in part because of higher value of Ω_b and in part due to their neglect of the photoheating and ionizing processes.

4.3. *X-Ray Background Radiation*

We have calculated the mean UV/X-ray background radiation field as a function of frequency as well as time including absorption by hydrogen and helium and both free-free and bound-free emission processes. Figure 7 shows the results at five epochs, $z = 5$ (*solid line*), $z = 3$ (*dotted line*), $z = 2$ (*short-dashed line*), $z = 1$ (*long-dashed line*), ($z = 0.5$ (*dotted, short-dashed line*) and $z = 0$ (*dotted, long-dashed line*). Emissivities from both $L = 64h^{-1}$ Mpc and $L = 16h^{-1}$ Mpc runs are included. The box in the middle shows the observational data by Wu et al. (1990). We see that the computed CDM model fails by a factor of 13 to produce the observed soft X-ray (0.2 to 1 keV range) background. The deficit at harder X-rays (1 to 10 keV range) is even larger (note that at the high-frequency end the computed spectrum has a very steep slope).

We find (not shown) that in the $L = 4h^{-1}$ Mpc box there are more ionizing photons than in any other box of our four runs. The reason is that shocks in this run leave a lot of baryonic matter at temperature around 10^5 K due to lack of large-scale power (which would have heated the matter to even higher temperatures were it present), which is optimal for producing UV ionizing photons. In this box, at redshift $z \leq 3$ the radiation from small-scale shocks is sufficient to maintain $J_{-21}(\nu) = 0.1$ at the Lyman limit (13.6 eV).

The strong edges seen in the spectra at 13.6 eV are due to absorption of neutral hydrogen. Meantime, the edges at the 54.4 eV absorption edge due to once-ionized helium is less significant simply because there is much less of this species. The edge at the ionization potential of neutral helium, 24.6 eV, is seen at early epochs, but is smaller because the 24.6 eV edge is too close to the L_α 13.6 eV edge to be very noticeable at our displayed resolution given the redshift smearing. At $z = 0$, hydrogen and helium are still not completely ionized, the troughs all remain. Again one should be reminded that energy feedback (e.g., UV and supernova processes) from star formation was not included in the simulations.

Figure 8*a* shows the fractions of H I (*solid line*), H II (*dotted line*), He I (*short-dashed line*), He II (*long-dashed line*), and He III (*short, long-dashed line*) in terms of their corresponding species as a function of redshift for the $L = 64h^{-1}$ Mpc box. Figure 8*b* shows the ionization history in this CDM model; we have removed the collapsed baryonic mass from this calculation, since that mass would presumably have formed into stars and the gaseous opacity of that material is thus irrelevant.

TABLE 4

SUMMARY OF FRACTIONS IN THE $L = 1h^{-1}$ Mpc BOX MODEL

Redshift	Z 10	5	3	2	1	0
A. Volume Weighted Fractions						
(1) "Virialized Gas"	0	0.000000	0.000007	0.000004	0.000011	0.000008
(2) "Galaxies"	0.	0.000002	0.000003	0.000006	0.000006	0.000002
(3) "Hot IGM"	0.	0.000000	0.000026	0.000000	0.000000	0.002432
(4) "Voids"	1.	0.999998	0.999990	0.999990	0.999982	0.997557
B. Mass-Weighted Fractions						
(1) "Virialized Gas"	0.	0.000001	0.002088	0.001939	0.011562	0.026717
(2) "Galaxies"	0.	0.001001	0.011268	0.018725	0.054532	0.069656
(3) "Hot IGM"	0.	0.000000	0.000000	0.000000	0.000000	0.000462
(4) "Voids"	1.	0.998998	0.986644	0.979335	0.933906	0.903166

TABLE 5

MASS FRACTION AND AVERAGE MASS OF COLLAPSED OBJECTS IN THE FOUR MODELS

L (h^{-1} Mpc)	$\langle m \rangle$ ($M_\odot$)	f (collapsed)
64	5.3×10^{10}	0.03
16	1.8×10^{9}	0.07
4	1.1×10^{9}	0.08
1	1.5×10^{8}	0.05

However, this removal does not make any noticeable difference in the computed quantities. Note how the optical depth in L_α (Gunn-Peterson) at redshift 4–5 is approximately 2×10^5, is about six orders of magnitude higher than the value 0.35 at $z = 4.2$ obtained from observations of high-redshift quasars by Jenkins & Ostriker (1991). Also shown are the optical depth due to He II L_α and He I L_α at 0.584 μ. Interestingly, the universe is optically thin for radiation in the 24.6 to 54.4 eV window before $z = 4$. The reasons are the following: only a very small fraction of He II is present at that time and hydrogen absorption is not efficient in this wavelength range. But after $z = 4$, enough He II is produced to make the universe opaque.

In order to compare more precisely with QSO absorption spectrum we also computed the average depression of the radiation field D_A shortward of L_α due to L_α lines. This is calculated as

$$D_A \equiv -\ln(\langle e^{-\tau_{\rm H}} \rangle) , \tag{6}$$

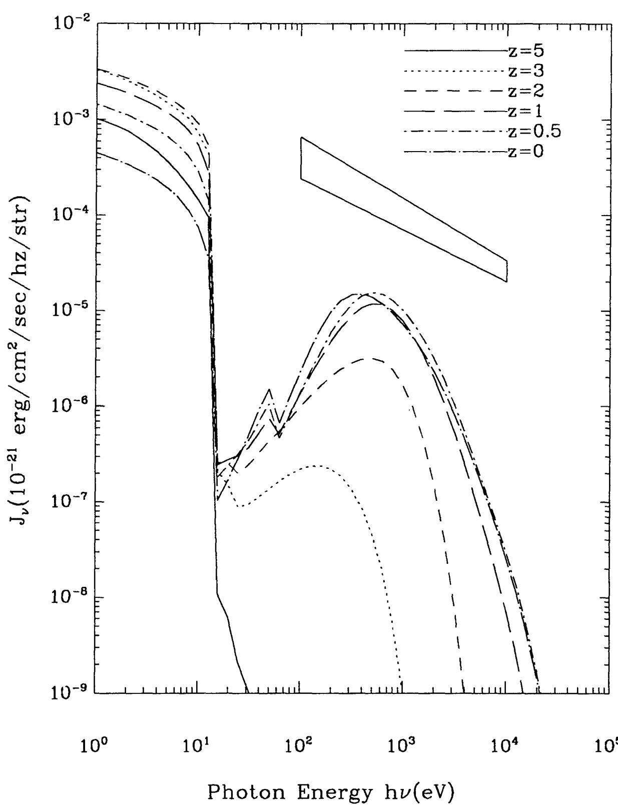

FIG. 7.—Mean radiation at five epochs, at $z = 5$ (*solid line*), $z = 3$ (*dotted line*), $z = 2$ (*short-dashed line*), $z = 1$ (*long-dashed line*) and $z = 0$ (*dotted-dashed line*). The box in the middle shows the observational data by Wu et al. (1990).

where the angular brackets indicate averaging over the cells of the simulation box, and $\tau_{\rm H}$ is the L_α optical depth of a cell. Figure 8*c* shows the computed $1 - D_A$ due to L_α (*solid line*), the observed quasars (*open dots*) and the least-squares fit of the observed data (*dotted line*); taken from Jenkins & Ostriker (1991). It is very obvious that CDM is far from satisfying the Gunn-Peterson test of the high-redshift quasar observations, i.e., the IGM cannot be ionized by means of shock heating, bremsstrahlung and free-bound radiation. Radiation from star formation might in principle eliminate this discrepancy and in fact, in our subsequent preliminary work which includes stellar UV luminosity, the problem is alleviated.

4.4. *Zel'dovich-Sunyaev Effect*

Now we turn to the results of the mean Zel'dovich-Sunyaev y parameter at several epochs, $z = 5$, 3, 2, 1, 0.5, 0, which are listed in Table 6. Most of the contribution to the Zel'dovich-Sunyaev effect comes from the epoch between $z = 1$ to $z = 0$ for two reasons. First, the path of a photon is longer at later times. Second, the temperature of the baryonic matter is higher at later epochs. Table 6 shows the directly computed value of the y parameter. Due to our inevitable numerical inadequacies we have underestimated $\langle y \rangle$. Using the extrapolation formula derived in Cen (1992a) (cf. eq. [76] of that paper), if we had included all the waves and had infinite resolution in the calculation, we would have obtained the following extrapolated value and an estimated fluctuation of y at $z = 0$ when (N^{-1}, $L_{\rm max}^{-1}$, $L_{\rm min}) \rightarrow 0$, $\langle y \rangle = (1.1 \pm 0.6) \times 10^{-6}$, $\langle \delta y \rangle = (1.2 \pm 0.6) \times 10^{-6}$ on arcminute scales (where the "$\pm$" indicates our estimate of the error of our extrapolation procedure). If the reader distrusts our extrapolation procedure, then Table 6 can be taken as a firm lower bound on $\langle y \rangle$ for the adopted model.

Bond (1990) calculated theoretical maps of CBR anisotropies using $P(k)$, linear theory and simple physics. He obtained $\langle y \rangle = 2 \times 10^{-6}$ and $\langle \delta y \rangle = 3 \times 10^{-6}$ on arcminute scales, which is in rough agreement with our result (note he uses $b = 1.4$, $\Omega_b = 0.1$, and we use $b = 1.5$, $\Omega_b = 0.06$). If we had used the same set of parameters as Bond did, given the scaling $y \propto \Omega_b b^{-4.6}$ (cf. Cen et al. 1990), the scaled values would have been $\langle y \rangle = (2.5 \pm 1.3) \times 10^{-6}$, $\langle \delta y \rangle = (2.8 \pm 1.9) \times 10^{-6}$ on arcminute scales. The fluctuation pattern on arcminute scales must be non-Gaussian; since these scales are very nonlinear at present, the proper maps of these fluctuations should be obtained by nonlinear numerical simulations. The detailed fluctuations of CBR due to this effect will be treated in a later paper.

We compare here this effect with the Sachs-Wolfe effect (Sachs & Wolfe 1967). The fluctuations to the CBR due to gravitational redshift and Doppler redshift due to density fluc-

TABLE 6

MEAN ZEL'DOVICH-SUNYAEV y-PARAMETER AS A FUNCTION OF REDSHIFT

Redshift (z)	$\langle y \rangle$
5	2.6×10^{-10}
3	2.6×10^{-9}
2	1.2×10^{-8}
1	4.0×10^{-8}
0.5	1.8×10^{-7}
0	5.5×10^{-7}

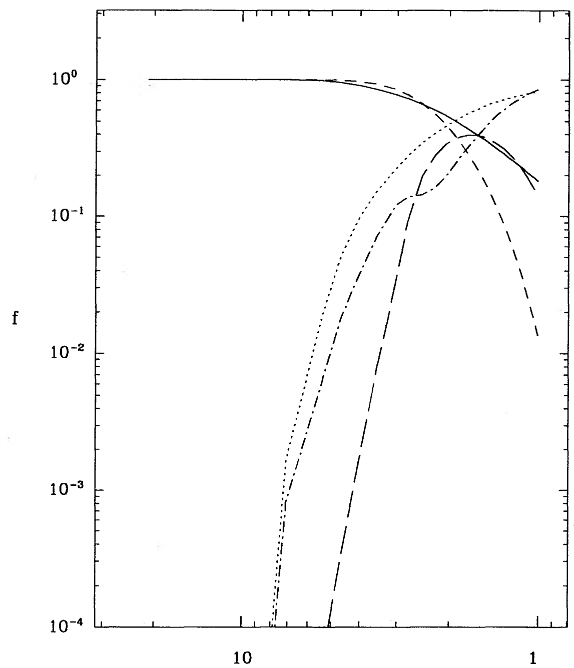

FIG. 8*a*

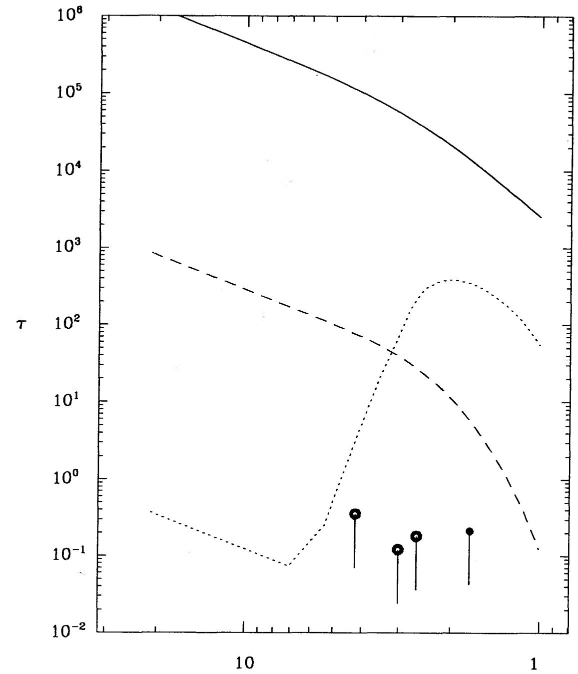

FIG. 8*b*

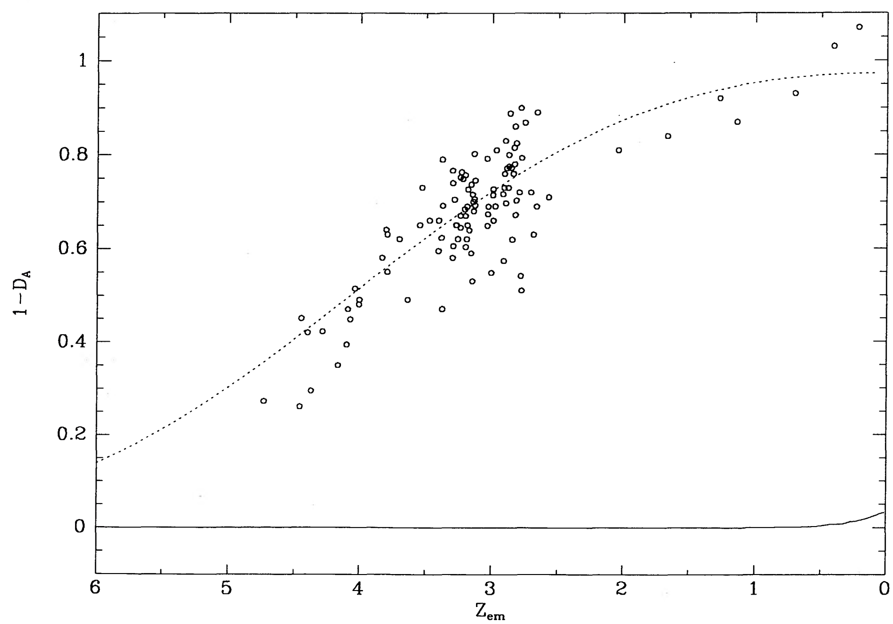

FIG. 8*c*

FIG. 8.—Ionization history of the CDM model. (*a*) Fraction of H I (*thick solid line*), fraction of H II (*thick dotted line*), fraction of He I (*thin solid line*), fraction of He II (*thin dotted line*) and fraction of He III (*thin dashed line*). (*b*) Solid line is the optical depth at the hydrogen L_α, i.e., Gunn-Peterson optical depth as a function of redshift. The dotted and dashed lines are the corresponding He II L_α optical depth and He I 0.584μ optical depth. The open circles with a vertical short line are the observational upper limit data at $z = 4.2$, 3.0, 2.6 by Jenkins & Ostriker (1991) for hydrogen L_α more than six orders of magnitude below the computed curve. The filled circle with a vertical short line is the observational upper limit data at $z = 1.722$ by Tripp, Green, & Bechtold (1990) for He I L_α. (*c*) Computed $1 - D_A$ due to L_α (solid line), the observed quasars (*open dots*) and the least-squares fit of the observed data (*dotted line*). It is very obvious that CDM is far from satisfying the Gunn-Peterson test of the high-redshift quasar observations.

tuations in the large-scale mass distribution are simply (Bond 1988)

$$\frac{\Delta T_R}{T_R} = \frac{\phi}{3}, \tag{7}$$

where ϕ is the gravitational potential fluctuations, which is roughly constant on the scales $\geq 10'$. Bond & Efstathiou (1984) (also see Vittorio & Silk 1984) made a detailed calculation for CDM model on scales $\geq 1'$ adopting the following set of parameters: $\Omega = 1$, $\Omega_b = 0.03$, $h = 0.75$ and $b = 1.0$. They found that at a scale of $1'$, $\Delta T_R/T_R = 2.0 \times 10^{-7}$ (cf. their Fig. 1) with the decrease due to smoothing at scales smaller than the thickness of the last scattering surface. If we corrected the difference of our $b(= 1.5)$ from their $b = 1.0$, their calculated value for our adopted CDM model due to Sachs-Wolfe effect would be $\Delta T_R/T_R = 1.3 \times 10^{-7}$, which translates to $y = 6.5 \times 10^{-8}$. This value is about a factor of 17 lower than the lower bound we find for the Zeldovich-Sunyaev effect.

4.5. *Galaxy and Dark Matter Correlation Functions*

A cell belonging to the second category defined in § 4.2 is called a galaxy. Further, such cells, if adjacent, are grouped into a single "isolated galaxy" although at our resolution we cannot tell the difference between galaxies and small groups such as the Local Group. We have found 1118 such "isolated galaxies" at $z = 1$ in the $L = 64h^{-1}$ Mpc box. The reason we identify the galaxies at $z = 1$ instead of $z = 0$ is that the breaking of long waves at later times heats up the baryonic matter causing evaporation of earlier identified galaxies. In a more realistic calculation (now in progress) the transition to collisionless (stellar) material would be irreversible. We note that, given our poor spatial resolution, many of our "galaxies" could be small groups such as the Local Group. We also randomly selected 2900 dark matter particles over the whole box ($L = 64h^{-1}$ Mpc box) at $z = 1$, which is a good approximation for the representation of the total mass distribution.

Figure 9 shows the galaxy-galaxy as well as dark matter particle-particle two-point correlation functions in the simulation with box size $L = 64h^{-1}$ Mpc at $z = 1$. Open and filled circles are the galaxy-galaxy and dark matter particle-particle two-point correlation functions, respectively; the dotted line, $\xi(R) = (R/5h^{-1}\ \mathrm{Mpc})^{-1.8}$, is the observational data for galaxies (cf. Davis & Peebles 1983) scaled down by a factor of $1/(1 + z)^2 = \frac{1}{4}$ appropriate to redshift $z = 1$. It shows that the galaxy distribution is biased over the mass distribution with the bias factor of about 2. Even more amazingly the slope of the galaxy-galaxy correlation function lies just on the observational data. To calculate the bias parameter more accurately, we performed the following computation. With the positions of the galaxies at $z = 1$, every galaxy is assigned the same mass, then we use the cloud-in-cell scheme to assign the galaxy density to the grid. Next, we use the FFT to transform the galaxy density field to Fourier space, there we compute the power spectrum of this galaxy density field, then multiply this spectrum by a top-hat sphere window function of radius $8h^{-1}$ Mpc. By integrating it in three-dimensional k space we finally obtain the galaxy number density fluctuations on a top hat sphere of radius $8h^{-1}$ Mpc, $(\Delta N/N)^2_{\mathrm{rms}}$. Using this definition we find that $(\Delta N/N)_{\mathrm{rms}} = 0.77$ at $z = 1$. Using the same procedure, we find that $(\Delta M/M)_{\mathrm{rms}} = 0.40$. By definition, bias is $b \equiv (\Delta N/N)_{\mathrm{rms}}/(\Delta M/M)_{\mathrm{rms}}$. This shows that the derived b for galaxies is 1.9 at $z = 1$.

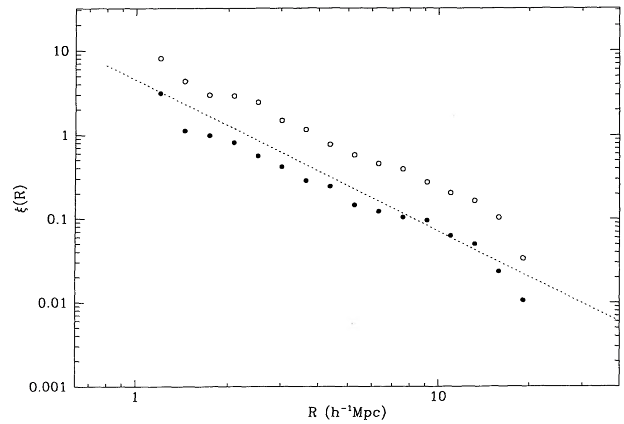

FIG. 9.—Galaxy-galaxy as well as dark matter particle-particle two-point correlation functions in the simulation of $L = 64h^{-1}$ Mpc box at $z = 1$. Open and filled circles are the galaxy-galaxy two-point position correlation and the dark matter particle-particle two-point position correlation, respectively, the dotted line is the observational data (cf. Davis & Peebles 1983), $\xi(R) = (R/5h^{-1}\ \mathrm{Mpc})^{-1.8}$ scaled down by a factor of $1/(1 + z)^2 = \frac{1}{4}$. Note that the simulated galaxies are positively biased with regard to the dark matter and the observed galaxies.

We expect that the mass fluctuations will grow faster than the galaxy number fluctuations from $z = 1$ to $z = 0$, i.e., the galaxy number density fluctuations would increase less rapidly than the mass fluctuation (which are essentially in the linear growth regime at the $8h^{-1}$ Mpc scale from $z = 1$ to $z = 0$) mainly because a smaller number of galaxies will form during this period and these galaxies will be more uniformly distributed than earlier formed galaxies, so we expcct that a bias of about 1.5 will survive in the end. Our preliminary results on improved runs with collisionless galaxies show that the right amount of bias (about 1.5) is maintained at the end ($z = 0$), consistent with the value we initially used to fix the amplitude of the power spectrum. The bias factor we have found is consistent with what was found in Ryu et al. (1990) ($b = 1.3$ to $b = 1.7$) who used a simple overdensity criterion.

4.6. *Mass Functions and Multiplicity Functions*

A cell is called a bound cell if it satisfies the following criteria:

$$\phi + 0.5(v^2 + C^2) < -0.5v_b^2, \tag{8}$$

where ϕ is the proper peculiar gravitational potential; v is the proper peculiar velocity; C is the local speed of sound. We take $v_b^2 \equiv 141^2\ (\mathrm{km\ s^{-1}})^2$; here v_b^2 is the binding energy per uniit mass. We choose such a value of v_b to satisfy the requirement that about 70% of the galaxies are in groups/clusters as observations indicate (Gott & Turner 1977, Fig. 2). The definition we have used is arbitrary but corresponds roughly to what observers identify as "bound groups." Of course in an $\Omega = 1$ universe *all* galaxies are bound to all other galaxies. After we have found these bound cells, we group them into a number of "groups" within each group all the cells are connected (i.e., touching by at least one side of a cell). The multiplicity function of the bound groups, which are defined above, is shown in Figure 10.

Figure 11 shows the baryonic and total mass/multiplicity functions of collapsed objects. Open triangles, filled dots, filled triangles, and filled squares are collapsed objects from four different boxes, with box sizes $L = (64, 16, 4, 1)h^{-1}$ Mpc,

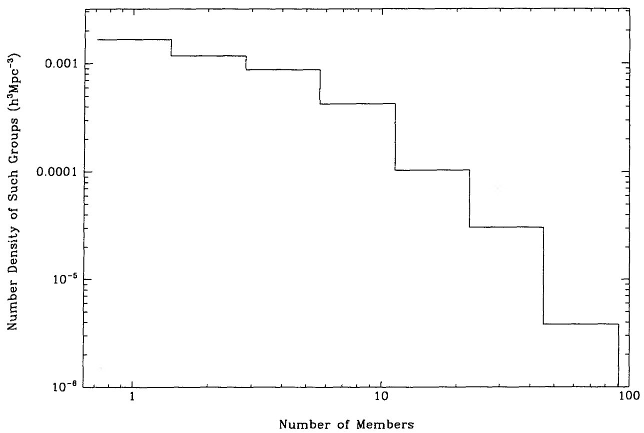

FIG. 10.—Number density of groups as functions of number of galaxies in the group identified in the $L = 64h^{-1}$ Mpc box. This is related to the multiplicity function but a quantitative comparison with observations is not appropriate given our poor spatial resolution.

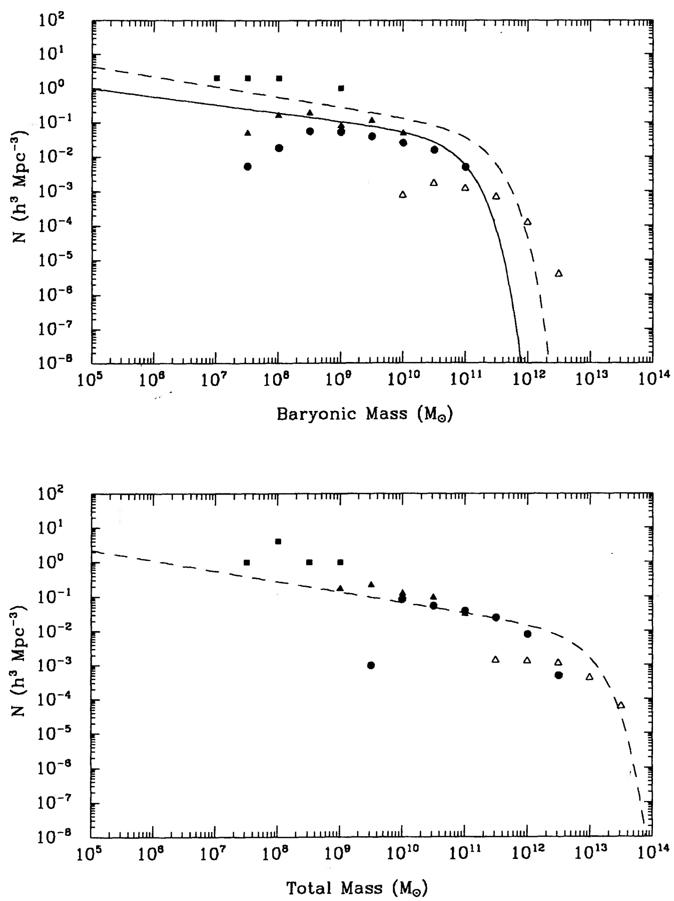

FIG. 11.—Baryonic and total mass/multiplicity functions of collapsed objects. Open triangles, filled dots, filled triangles, and filled squares are collapsed objects from four different boxes, with box sizes $L = (64, 16, 4, 1)h^{-1}$ Mpc, respectively. (*upper panel*) Baryonic mass/multiplicity function of collapsed objects; the dashed line is a fitting formula (eq. [9]), where $M_{\rm baryon}$ is in units of solar mass, the solid line is the derived Schechter function if mass to light ratio is 4.2 (eq. [12]). (*lower panel*) Total mass/multiplicity function of collapsed objects, and the dashed line is a fitting formula (eq. [10]). Data fit the Schechter function if the baryon mass to blue light ratio is in the range 1.5–7.7.

respectively. As noted earlier the results in the smaller boxes overestimate the amount of bound material. The upper panel shows the baryonic mass/multiplicity function of collapsed objects, and the dashed line is a fitting formula (eq. [9]). The lower panel shows the total mass/multiplicity function of collapsed objects, and the dashed line is a fitting formula (eq. [10]). We applied a simple fitting formula to describe the (simulated) data for the number of galaxies number per h^{-3} Mpc^3 per unit interval of the corresponding (baryonic or total) mass

$$f(M_{\rm bar})dM_{\rm bar} = 0.06\left(\frac{M_{\rm bar}}{M^*_{\rm bar}}\right)^{-1.3} e^{-M_{\rm bar}/M_{\rm bar}*} d\left(\frac{M_{\rm bar}}{M^*_{\rm bar}}\right) \quad (9)$$

Here $M_{\rm bar}$ is the baryonic mass in units of solar mass, $M^*_{\rm bar} = 1.5 \times 10^{11}\, M_\odot$.

$$f(M_{\rm tot})dM_{\rm tot} = 0.01\left(\frac{M_{\rm tot}}{M^*_{\rm tot}}\right)^{-1.3} e^{-M_{\rm tot}/M_{\rm tot}*} d\left(\frac{M_{\rm tot}}{M^*_{\rm tot}}\right), \quad (10)$$

where $M^*_{\rm tot} = 5 \times 10^{12}\, M_\odot$.

Schechter (1976) gave an approximate formula for the luminosity function of galaxies as follows:

$$\phi(L)dL = \phi^*\left(\frac{L}{L^*}\right)^{\alpha} e^{-L/L^*} d\left(\frac{L}{L^*}\right), \quad (11)$$

where $\phi(L)dL$ is the number density of galaxies per cubic Mpc in the luminosity interval L to $L + dL$. He found that with $\alpha = -1.24 \pm 0.19$, $M^*_{B(0)} = -20.60 \pm 0.11$ and $\phi^* V^* = 216 \pm 6$, and subsequent work has not very much altered the best fit to the observed data. Comparing equations (9) and (11), we can now see if a self-consistent value for the mass to light ratio can be found by matching the two fits. Schechter's (1976) paper assumes, as we do, that $h = 0.5$. He found $V^* = 4.3 \times 10^4$ Mpc^3, which fixes ϕ^* to be 5.0×10^{-3}. Now from equation (9) we know than $f(M^*_{\rm bar}) = 0.06h^3$, so we can obtain the first estimate of the baryonic mass to blue light ratio to be $(M/L)_1 = 0.06h^3/(5 \times 10^{-3}) = 1.5$. We obtain a second baryonic mass to light ratio by matching the fiducial luminosity of $L^*_{B(0)} = 1.3 \times 10^{10}\, L_\odot$ with $M^*_{\rm bar}$, which ratio found to be $(M/L)_2 = 1.5 \times 10^{11}/1.3 \times 10^{10} = 11.5$. The second estimate is somewhat higher than the first one, in part due to the low resolution of our simulations. For example, we are not able to resolve a system like the Local Group; we treat all objects in this system as one galaxy. It is interesting that these estimates are roughly consistent with one another and both are not far from what is obtained in the Galactic disk via the Oort limit or in globular cluster with the virial theorem. If we take the geometric average of these two estimates, $(M/L) = 4.2$, and substitute into equation (11), we obtain the derived Schechter mass function as follows:

$$\phi(M)dM = 0.04\left(\frac{M}{M^*}\right)^{-1.24} e^{-M/M^*} d\left(\frac{M}{M^*}\right), \quad (12)$$

where $M^* = 5.4 \times 10^{10}\, M_\odot$. This is shown as the solid line in upper panel of Figure 11. In so far as the solid line fits the computations, we can say that the derived mass functions for collapsed baryonic matter are consistent with observations when a baryonic mass to light ratio of 4–5 is adopted.

4.7. *X-Ray Clusters Luminosity Function and its Evolution*

Our computation allows us to estimate what the local cluster X-ray luminosity function would be in this CDM model. We calculate the X-ray luminosities in two different bands: (1) 0.3–3.5 keV and (2) 0.5–4.5 keV. Figure 12*a* shows the number density of the most luminous hard X-ray spots within an inner sphere of radius $0.5h^{-1}$ Mpc in band (2) in the $L = 64h^{-1}$ Mpc box. The dotted line is the observational data in X-ray band (2) by Giacconi & Bury (1989). One may note that the CDM model does not seem able to produce enough X-ray clusters although our numerical inaccuracy must have exaggerated the discrepancy.

Figure 12*b* shows the number densities of most luminous X-ray regions in band (1) at $z = 0$, $z = 1$, and $z = 2$. The thin dotted, short-dashed and long-dashed lines are the observations by Gioia et al. (1990) at $z = 0.14$–0.20, $z = 0.20$–0.30, and $z = 0.30$–0.60, respectively. The computed model shows a negative evolution from $z = 2$ to $z = 0.5$ and a positive evolution from $z = 0.5$ to $z = 0$. Evrard (1990) made a specific simulation aiming to understand the properties of rich X-ray clusters. He found that a total 2–10 keV luminosity of 7.5×10^{44} ergs s^{-1} is emitted at $z = 0$ for a simulated cluster like the Coma cluster, which is considerably higher than our result (see Fig. 12*b*) (a factor of 100). The different values of Ω_b adopted (0.1 in his case and 0.06 in our case) could narrow the difference down to a factor of 36, and a numerically improved simulation of ours would increase our computed cluster X-ray luminosity by a factor of at least 3, further reducing the difference to a factor of ≤ 12. The remaining difference could be due to different normalization, for example, in his simulation, a DC component is added to the density field, i.e., the average density of the simulated volume is greater than the mean cosmological background density. In Evrard's model, a peak height of 4.3 σ is simulated. The expected abundance of peaks of this height or higher is $n = 9 \times 10^{-9} h_{50}^3$ Mpc^{-3}. In our simulated $L = 64h^{-1}$ Mpc box, the probability of finding such a peak is $(64/0.5)^3 \times 9 \times 10^{-9} = 0.019$. Therefore, we do not expect to find such rich clusters in our simulation volume, and the obtained results are not inconsistent with that in Evrard (1990). In Figure 12*c* we show the projected pictures on to the three directions of our box of the above X-ray spots. The clustering of luminous X-ray regions is clearly seen; big voids ($\sim 30h^{-1}$ Mpc) are also visible.

5. CONCLUSIONS

Our hydrodynamic simulations of the CDM scenario utilizing different cell sizes and box sizes to cover the dynamic ranges of interest are sufficiently accurate, we believe, to allow us to compute, with reasonable confidence, properties of the gas distribution on scales larger than three cell sizes. On balance, our results tend to support the CDM scenario in so far as we find that our simulated "galaxies" agree far better with real observations than expected. That is, many of the objections to CDM, based on linear theory or dark matter only simulations, are lessened or removed if our simulations are valid. Of course some serious objections remain and other ones (such as the cluster X-ray luminosity function) are apparently made more stringent by this work.

1. For the CDM models with our chosen normalization, the soft X-ray radiation is far below and thus consistent with the observations by Wu et al. (1990). Much of the background is in fact produced by identifiable AGN sources. Furthermore, for purely numerical reasons, we know that with the same input parameters, a better treatment with larger N, larger $L_{\max}$ and smaller $L_{\min}$, would increase the X-ray output. A factor of 3 increase was found at 1 keV in the tests we made in Cen (1992a) for a 128^3 CDM run with $L = 64h^{-1}$ Mpc, $h = 0.5$, $b = 1.0$, $\Omega = 1$, and $\Omega_b = 0.1$. Finally, there would be quite significant fluctuations in the X-ray background in our models (treated in a later paper), possibly in conflict with observations if hot gas provided a large fraction of the background, once again indicating an upper bound. Given these facts, and the scaling that $J_x \propto b^{-4.3}\Omega_b^2$, we conclude that for CDM ($h = 0.5$) normalized to $(\Delta M/M)_{\rm rms} = 1/b$ at $8h^{-1}$ Mpc at $z = 0$, there is upper bound of

$$\Omega_b \leq 0.09 b^{2.2} \quad (h = 0.5) . \tag{13}$$

If we further correct for sources (at least half of the X-ray background radiation is due to discrete AGN sources) and numerical effects (a factor of at least 3 increase in our computed radiation field if higher resolution simulation is made) this limit is lowered to

$$\Omega_b \leq 0.037 b^{2.2} \quad (h = 0.5) , \tag{14}$$

a value which is consistent with the one we assumed in the computations and the latest nucleosynthetic values ($0.06h_{50}^{-2}$) (Walker et al. 1990; Schramm 1991). With our best estimate of $b = 1.5$ this limit becomes $\Omega_b < 0.09$. The extrapolation to a perfect simulation has an estimated error of not more than $\sqrt{2}$ so the error in equations (13) and (14) is estimated at $\pm(2^{1/4}-1) \sim \pm 20\%$.

2. Zel'dovich-Sunyaev Effect. The model has y parameters $\langle y \rangle = (1.1 \pm 0.6) \times 10^{-6}$ with fluctuations $\langle \delta y \rangle = (1.2 \pm 0.6) \times 10^{-6}$ on arcminute scales, which are potentially detectable by planned experiments given the fact that the effect has a non-Gaussian distribution.

3. Baryonic matter is biased over dark matter on small scales ($\leq 0.13h^{-1}$ Mpc) and antibiased on large scales ($\leq 0.13h^{-1}$ Mpc). A summarized table of the rms density fluctuations on cell scale of each run at $z = 0$ for four CDM models is shown in Table 7. The values on the right side of the arrows are estimated, extrapolated values after correction for numerical diffusion. We speculate that baryonic matter distribution is biased over dark matter distribution on scales $r \leq 0.13h^{-1}$ Mpc, and antibiased on scales $r \geq 0.13h^{-1}$ Mpc, while approaching to zero-bias on very large scales, say, $r \geq 10h^{-1}$ Mpc. Within an $8h^{-1}$ Mpc sphere we find that our simulated galaxies are biased by a factor of approximately 1.9 over the matter density at $z = 1$.

4. Using physical criteria for the formation of galaxies from cooling gas, we find that approximately the correct total mass density of baryons collapses to galaxies and that these have approximately the correct mass spectrum. Specifically, a reasonable fit to the observed Schecter luminosity function is obtained if $M_b/L_B = 4$ to give $M^*_{\rm bar} = 5 \times 10^{10}\ M_\odot$ and $M^*_{\rm tot} = 5 \times 10^{12}\ M_\odot$. Thermal energy prevents the smallest scales from being most unstable with a result that the mass-

TABLE 7

SUMMARY OF rms DENSITY FLUCTUATIONS ON CELL SIZE SCALE OF EACH MODEL

ΔL (h^{-1} Mpc)	σ (Baryonic Matter)	σ (Dark Matter)
0.5000	$3.9 \rightarrow 4.4$	5.4
0.1250	$8.7 \rightarrow 9.8$	9.8
0.0313	$62.3 \rightarrow 70.4$	12.5
0.0078	$105.4 \rightarrow 119.1$	15.4

NOTE.—$z = 0$.

weighted mass function is expected to decline for galaxy masses (in baryon) less than $2 \times 10^9 M_\odot$.

5. The CDM model can accurately reproduce the galaxy-galaxy two-point correlation, and is self-consistent in the sense that the bias factor we initially used to fix the amplitude of the power spectrum was approximately reproduced in the end.

6. Hydrogen is not fully ionized even at $z = 0$, so CDM fails to satisfy the Gunn-Peterson test of high-redshift quasars by itself, i.e., without other ionizing sources; shock heating and bremsstrahlung radiation as well as free-bound radiation from primordial baryonic matter in this model are not enough. Radiation from star formation might eliminate the difficulty

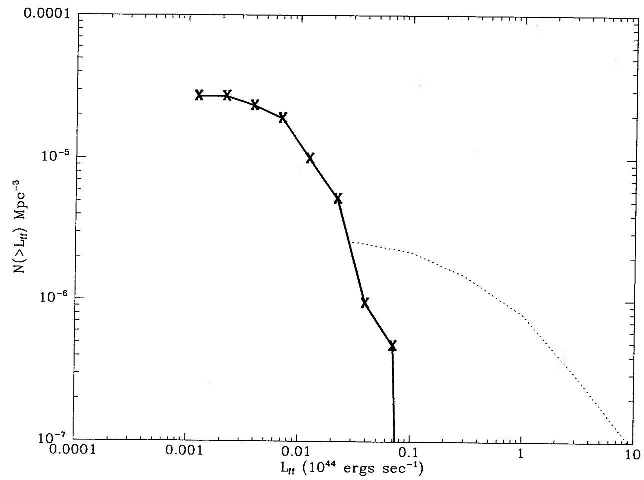

FIG. 12*a*

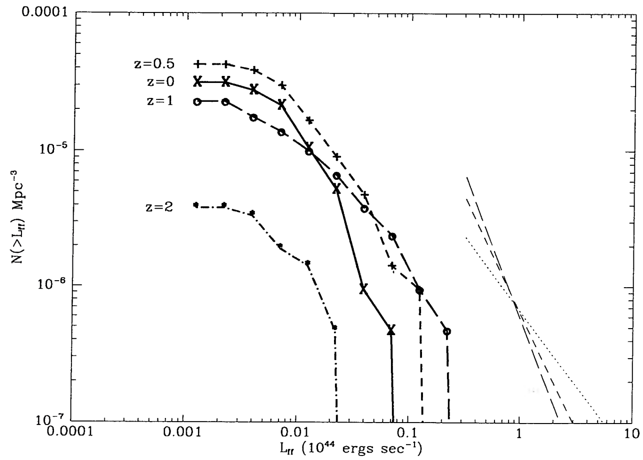

FIG. 12*b*

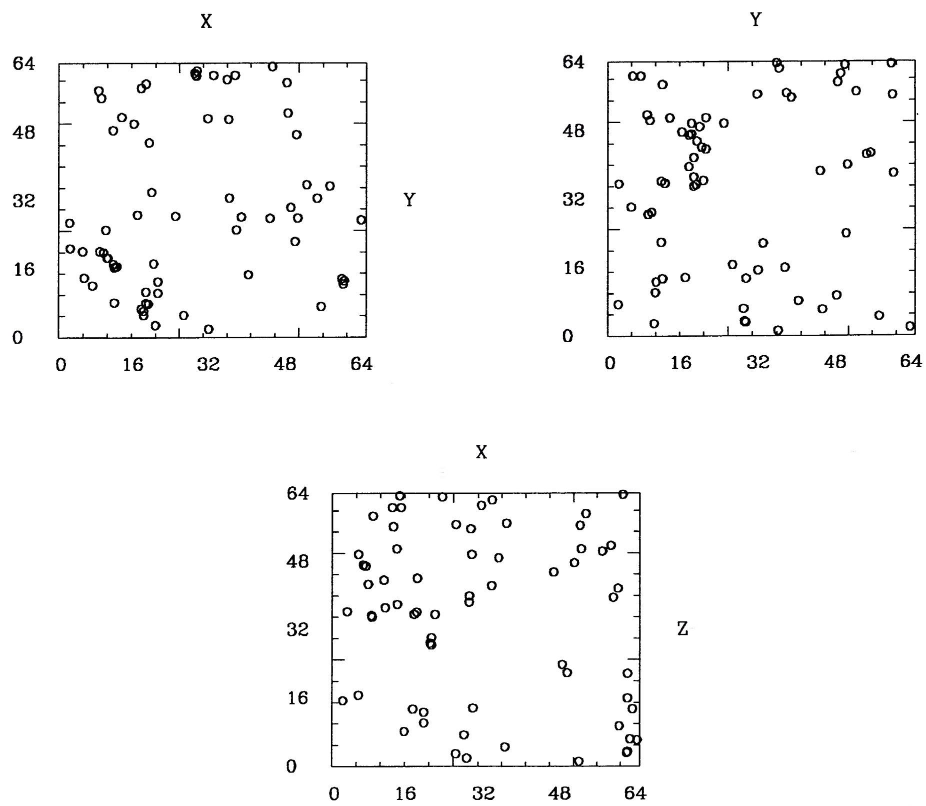

FIG. 12*c*

FIG. 12.—(*a*) Number density of most luminous hard X-ray spots within an inner sphere radius of $0.5h^{-1}$ Mpc of the model with box size $L = 64h^{-1}$ Mpc in band (2). The dotted line is the observational data in X-ray band (2) by Giacconi & Bury (1989). One may note the CDM model is not able to produce enough X-ray clusters. (*b*) Number densities of most luminous hard X-ray in band (1) at $z = 0$ (*cross and thick solid line*); at $z = 1$ (*plus and thick short-dashed line*); and at $z = 2$ (*asterisk and thick long-dashed line*). The thin dotted, short-dashed, and long-dashed lines are the observations by Gioia et al. (1990) at $z = 0.14$–0.20, $z = 0.20$–0.30 and $z = 0.30$–0.60, respectively. The computed model shows a negative evolution from $z = 2$ to $z = 1$ and a positive evolution from $z = 1$ to $z = 0$. (*c*) Projected pictures on to the three directions of our box of the above X-ray spots.

and results in our subsequent preliminary work utilizing a more advanced code with star formation actually seems to alleviate this problem.

This paper was done in partial fulfillment of the requirement for a Ph.D degree at Princeton University. Additional details of the results can be obtained by writing to R. Y. Cen; some are given in the Ph.D thesis and can be obtained from UMI Dissertation Service. We are happy to acknowledge support from NASA grant NAGW-765 and NSF grant AST90-06958. The work would not have been possible had not A. Jameson made his highly developed aerodynamics code available for astrophysical applications. We would like to thank A. Jameson for letting us use his Convex 220 computer, also thank D. H. Weinberg for making his valuable various codes available to us and for his helpful discussions. The many discussions with B. T. Draine, G. Evrard, J. E. Gunn, J. Goodman, E. Loeb, J. Miralda-Escude, B. Paczynski, M. Strauss, and E. Turner were also very helpful as was the report of an anonymous referee.

REFERENCES

Babul, A. 1989, Ph.D. thesis, Princeton Univ.
Bardeen, J. M., Bond, J. R., Kaiser, M., & Szalay, A. S. 1986, ApJ, 304, 15
Blumenthal, G. R., Faber, S. M., Primack, J. R., & Rees, M. J. 1988, in The Early Universe: Reprints, ed. E. W. Kolb & M. S. Turner (Reading, MA: Addison-Wesley), 61
Bond, J. R. 1986, in Galaxies and Deviations from Universal Expansion, ed. B. F. Madore & R. B. Tully (Dordrecht: Reidel), 255
———. 1988, in The Early Universe, NATO Advanced Study Institute on the Early Universe, ed. W. G. Unruh & G. W. Semenoff (Dordrecht: Reidel), 283
———. 1990, preprint
Bond, J. R., & Efstathiou, G. 1984, ApJ, 285, L45
Carlberg, R. G., Couchman, H. M. P., & Thomas, P. A. 1990, preprint
Cen, R. Y. 1992a, ApJS, 78, 341
———. 1992b, ApJ, submitted
Cen, R. Y., Jameson, A., Liu, F., & Ostriker, J. P. 1990, ApJ, 362, L41
Cen, R. Y., Ostriker, J. P., & Peebles, P. J. E. 1992, ApJ, in preparation
Cen, R. Y., Ostriker, J. P., Spergel, D. N., & Turok, N. 1991, ApJ, 383, 1
Chiang, W. H., Ryu, D., & Vishniac, E. T. 1989, ApJ, 339, 603
Davis, M., & Peebles, P. J. E. 1983, ApJ, 267, 465
de Lapparent, V., Geller, M. J., & Huchra, J. P. 1988, ApJ, 332, 44
Efstathiou, G., Davis, M., Frenk, C. S., & White, S. D. M. 1985, ApJS, 57, 241
Evrard, A. E. 1990, ApJ, 363, 349
Frenk, C. S., White, S. D. M., Davis, M., & Efstathiou, G. 1988, ApJ, 327, 507
Giacconi, R., & Bury, R. 1989, in STScI Symp. 4, Clusters of Galaxies, ed. W. R. Oegerle, M. J. Fitchett, & L. Danly (Baltimore: STScI), 373
Gioia, I. M., Henry, J. P., Maccacaro, T., Morris, S. L., Stocke, J. T., & Wolter, A. 1990, ApJ, 356, L35
Gorski, K. M., Davis, M., Strauss, M. A., White, S. D. M., & Yahil, A. 1989, ApJ, 344, 1
Gott III, J. R., & Turner, E. L. 1977, ApJ, 216, 357
Groth, E. J., Juszkiewicz, R., & Ostriker, J. P. 1989, ApJ, 346, 558
Gunn, J. E., & Peterson, B. A. 1965, ApJ, 142, 1633
Hockney, R. W., & Eastwood, J. W. 1981, Computer Simulations Using Particles (New York: McGraw-Hill)
Jameson, A. 1989, Science, 245, 361
Jenkins, E. B., & Ostriker, J. P. 1991, ApJ, 376, 33
Maddox, S. J., Efstathiou, G., Sutherland, W. J., & Loveday, J. 1990, MNRAS, 242, 43P
Ostriker, J. P., & Suto, Y. 1990, ApJ, 348, 378
Park, C. B. 1990, MNRAS, 242, 59
Peebles, P. J. E. 1982, ApJ, 263, L1
———. 1987, Nature, 327, 210
Peebles, P. J. E., & Silk, J. 1990, Nature, 346, 233
Ryu, D., Vishniac, E. T., & Chiang, W. H. 1990, ApJ, 354, 389
Sachs, R. K., & Wolfe, A. M. 1967, ApJ, 147, 73
Schechter, P. 1976, ApJ, 203, 297
Schneider, D. P., Schmidt, M., & Gunn, J. E. 1991, AJ, 102, 837
Schramm, D. N. 1991, private communication
Shapiro, P. R., & Struck-Marcell, P. 1985, ApJS, 57, 205
Sunyaev, R. A., & Zeldovich, Ya. B. 1970, Ap&SS, 7, 13
———. 1972, A&A, 20, 189
Tripp, T. M., Green, R. F., & Bechtold, J. 1990, ApJ, 364, L29
Vittorio, N., Juszkiewicz, R., & Davis, M. 1986, Nature, 323, 132
Vittorio, N., & Silk, J. 1984, ApJ, 285, L39
Walker, T. P., Steigman, G., Schramm, D. N., Olive, K. A., & Kang, H. S. 1991, ApJ, 376, 51
Weinberg, D. H. 1989, Ph.D. thesis, Princeton Univ.
Weinberg, D. H., & Gunn, J. E. 1990, MNRAS, 247, 260
Wu, X., Hamilton, T., Helfand, D. J., & Wang, Q. 1990, preprint
Yang, J., Turner, M. S., Steigman, G., Schramm, D. M., & Olive, K. A. 1984, ApJ, 281, 493
Yuan, W., Centrella, J. M., & Norman, M. L. 1991, ApJ, 376, L29
Zeldovich, Ya. 1970, A&A, 5, 84